Politecnico di Torino

Department of Applied Science and Technology (DISAT)

Master's Degree in Materials Engineering for Industry 4.0

Integration and Validation of a Revised Ventilation System for ATLAS Racks' Cooling

Master's Thesis

Politecnico di Torino Supervisor

Prof. Stefano Zucca

Candidate

Sedef Zeynep Bas

CERN Supervisor

Gerardo Velazquez Gutierrez

Academic Year

2025–2026

Abstract

The ATLAS detector relies on a large electronic infrastructure requiring reliable thermal management to ensure stable operation of its readout and control systems. The cooling method of the ATLAS electronics racks is based on a closed-loop air-circulation system in which tangential turbines circulate air through air-water heat exchangers connected to the CERN chilled-water network.

The original turbine units currently used in the cooling system are no longer commercially available. Consequently, a replacement turbine configuration must be integrated while maintaining compatibility with the existing rack infrastructure and preserving cooling performance.

This thesis presents the integration and validation of a revised ventilation system for ATLAS electronics racks. The work includes CAD reconstruction of the turbine assemblies using existing digital models and reverse engineering techniques, the design of adaptation components, prototype assembly, simplified rotor dynamics analysis, development of an assembly procedure and experimental validation.

Experimental validation was performed through airflow and vibration measurements. Airflow measurements demonstrated that the revised turbine assembly maintained the cooling capability of the original system, achieving a volumetric flow rate comparable to and slightly higher than the previous configuration.

Initial vibration measurements revealed significantly higher vibration levels in the prototype. A systematic root-cause investigation was therefore conducted. The results demonstrated that the elevated vibration levels were primarily associated with the refurbished motor assemblies and assembly-related factors rather than the revised wheel design itself. Assembly preload, casing deformation, and local support conditions were found to significantly influence the measured vibration response.

Following implementation of controlled assembly procedures and correction of local support conditions, the revised wheel assembly was validated from a vibration point of view using healthy motor/case assemblies. The resulting vibration levels were comparable to those of the original system, demonstrating that the revised wheel assembly can be successfully integrated without introducing a significant vibration penalty.

In addition, an assessment of the available inventory was performed to define an optimized distribution of long and short chassis assemblies for future implementation while minimizing additional procurement.

The results demonstrate that the revised turbine system can be integrated into the ATLAS cooling infrastructure while maintaining airflow performance and achieving vibration levels comparable to the previous configuration. The remaining vibration optimization

opportunities identified during the study are primarily associated with the refurbished motor assemblies rather than the revised wheel design.

The outcomes of this work will be implemented by the ATLAS Technical Coordination team to support the refurbishment and maintenance of the plastic turbine ventilation system used in ATLAS electronics racks throughout the remaining operational lifetime of the LHC, currently planned until 2040.

Table of Contents

List of Figures

List of Tables

Glossary

ATLAS A Toroidal LHC ApparatuS detector experiment. 10

CERN European Organization for Nuclear Research. 9

LEP Large Electron-Positron Collider. 15

LHC Large Hadron Collider. 10, 15, 16

LS3 Long Shutdown 3 of the Large Hadron Collider upgrade programme. 10

Chapter 1

Introduction

1.1 CERN and the Large Hadron Collider

CERN, the European Organization for Nuclear Research, is an intergovernmental organization with over 30 Member States. Its seat is in Geneva but its premises are located on both sides of the French-Swiss border (https://maps.web.cern.ch/). CERN's mission is to enable international collaboration in the field of high-energy particle physics research and to this end it designs, builds and operates particle accelerators and the associated experimental areas. At present, more than 10000 scientific users from research institutes all over the world are using CERN's installations for their experiments.

The accelerator complex at CERN is a succession of machines with increasingly higher energies. Each machine injects the beam into the next one, which takes over to bring the beam to an even higher energy, and so on. The flagship of this complex is the Large Hadron Collider (LHC)[3] see Figure 1.1.

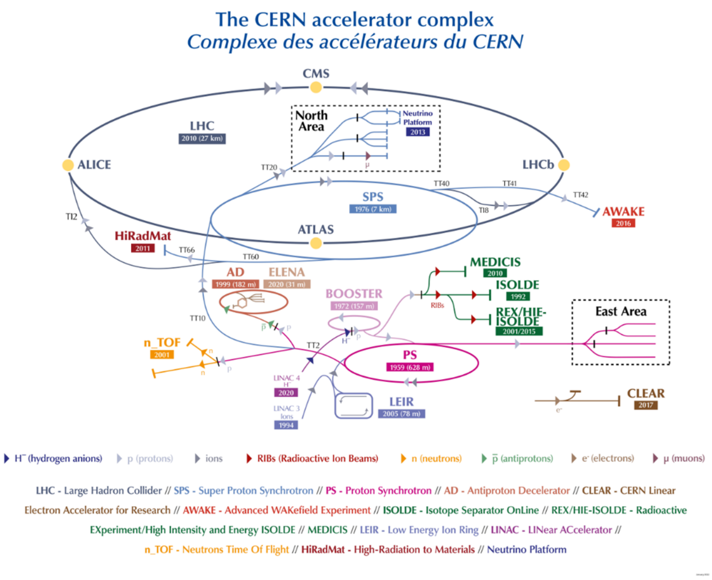

Figure 1.1: CERN Accelerator Complex [3]

1.2 The ATLAS Experiment

ATLAS,A Toroidal LHC ApparatuS detector experiment, is a particle physics experiment at the Large Hadron Collider (LHC) at CERN. The ATLAS detector is designed and constructed to make new particle discoveries resulting from head-on collisions of protons produced by the LHC of extraordinarily high energy. ATLAS will investigate the basic forces that have shaped our universe since the beginning of time and that will determine its fate. Among the possible discovery candidates are particles that could explain the origin of mass, confirm the existence of extra dimensions in space, unification of fundamental forces, and evidence of dark matter in our universe. The ATLAS detector is located in an underground cavern on the Swiss part of the CERN site. The experiment is in operation and produces physics results. The ATLAS collaboration involves more than 3000 scientists from 174 institutions in 38 countries.[1]

1.3 The Long Shutdown 3 Upgrade Programme

The operation of the LHC is organized in cycles consisting of physics data-taking periods followed by long shutdowns during which maintenance, consolidation and upgrade activities are performed. These shutdown periods are essential to ensure the long-term reliability of the accelerator complex and to allow the implementation of detector and infrastructure upgrades required for future physics programs.[5]

The third long shutdown of the LHC, referred to as Long Shutdown 3 (LS3), is scheduled to take place after the completion of Run 3 operations at the end of June 2026 and it is scheduled to last for 3 years. During LS3, major upgrade activities will be carried out across the CERN accelerator complex and within the LHC experiments in preparation for the High Luminosity LHC (HL-LHC) era. These upgrades aim to increase the luminosity delivered by the accelerator and to improve the performance and radiation tolerance of the experimental detectors.[5]

Within the ATLAS experiment, LS3 represents a major phase of detector and infrastructure upgrades. In addition to the installation of new detector components, several technical systems supporting detector operation must be adapted or upgraded in order to ensure reliable performance under the future operating conditions.

This thesis was developed in the context of upgrade activities for the ATLAS experiment during the preparation phase of Long Shutdown 3 (LS3).

1.4 Electronics Racks of ATLAS

The ATLAS detector relies on a large electronics infrastructure responsible for detector readout, data acquisition and control systems. These electronic systems are installed in dedicated racks that host multiple electronic modules operating continuously during detector operation. As a result, the electronics dissipate significant amounts of heat which must be removed efficiently in order to maintain stable operating temperatures and ensure reliable system performance.

The available cooling infrastructure in the ATLAS's cavern provides approximately 1000 kW of water cooling capacity, while the available HVAC cooling power is approximately 200 kW. Because the HVAC system has significantly lower capacity, the rack cooling system was designed so that the majority of the generated heat is removed through the water cooling infrastructure rather than through the experimental cavern's HVAC system.

These racks are installed in the experimental cavern of the ATLAS detector, where environmental conditions such as limited space, restricted access, and the presence of magnetic fields impose additional constraints on the design and operation of the cooling system. In particular, the presence of magnetic fields restricts the use of conventional metallic fans, leading to the use of plastic tangential fans for airflow generation.

Within the ATLAS Technical Coordination team, tangential fans are commonly referred to as turbines. Consequently, the terms "fan" and "turbine" are used interchangeably throughout this thesis when referring to these components.

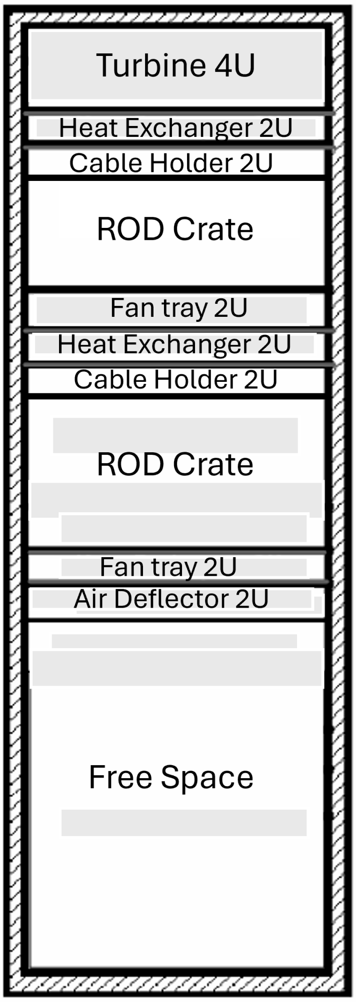

Figure 1.2: An example rack configuration

A more detailed description of the rack cooling system architecture and airflow configuration is provided in the following chapter.

1.5 Need for System Revision

The turbine units installed in the rack cooling system play a critical role in maintaining the airflow required for proper heat removal. However, the turbine model originally used in the system is no longer commercially available. Considering that these turbines have a typical operational lifetime of approximately five years, their replacement is required during maintenance and upgrade operations such as LS3.

A complete redesign of the rack cooling system would require significant modifications to the existing infrastructure and would introduce considerable complexity in terms of installation, cost, and validation. Therefore, a solution was sought that would allow the integration of a new turbine while preserving compatibility with the existing mechanical configuration.

A commercially available replacement turbine was selected. However, due to geometric differences between the original and the new turbine, direct integration into the existing assembly was not possible. In order to overcome these incompatibilities, necessary adaptation and joining components were engineered to ensure proper alignment between the motor shaft, turbine wheel, and bearing interfaces. These components enable the integration of the new turbine into the existing mechanical assembly while maintaining the required functionality and integrity of the rotor system.

1.6 Objectives of the Thesis

The main objective of this thesis is to investigate the mechanical integration and validation of a revised ventilation system for the ATLAS rack cooling infrastructure.

To achieve this objective, the following specific goals are defined:

- To reconstruct the CAD models of the turbine assembly by combining existing digital models with reverse engineering based on dimensional measurements of components lacking available documentation.
- To design and implement the necessary adaptation and joining components required to integrate the new turbine into the existing mechanical system.
- To develop a prototype configuration of the revised turbine system and define a consistent assembly procedure.
- To experimentally evaluate the airflow performance of the revised configuration and compare it with the expected performance of the original system.
- To assess the mechanical integrity of the turbine assembly under operational conditions, including structural considerations related to load transmission and component interaction.
- To analyze the available inventory and define an optimized distribution of "long" and "short" chassis configurations for future implementation, minimizing additional procurement requirements.

Chapter 2

Rack Cooling System Architecture

2.1 Rack Cooling Concept

The cooling of the ATLAS electronics racks is based on a closed-loop air circulation system combined with water-cooled heat exchangers. This design was selected in order to efficiently remove the heat generated by the electronics while minimizing the thermal load transferred to the experimental cavern. The cooling system operates using water supplied from the CERN chilled water network. In the current rack configuration, the inlet water temperature is 14 °C while the outlet temperature typically reaches around 20 °C, depending on the thermal load.

The cooling system is implemented in standard 19-inch electronics racks, which provide a modular and standardized framework for housing electronic subracks, cooling components, and associated infrastructure.

In this configuration, air inside the rack circulates in a closed loop. The air absorbs heat generated by the electronic modules and transports it through the water-cooled heat exchangers installed within the rack. At the heat exchanger interface, the thermal energy carried by the air is transferred to the cooling water circulating through the heat exchanger. The cooled air is then recirculated within the rack, allowing the process to repeat continuously during operation.

The electronic modules themselves are equipped with fan modules which assist in moving air vertically through the electronics. Air circulation within the rack is further ensured by tangential turbines installed in a dedicated mechanical chassis located at the top of the rack. The airflow generated by the module fans carries the heated air upwards toward the turbines. The tangential turbines then redirect the airflow toward the side channels of the rack. The circulating air subsequently reaches an air deflector located at the bottom of the rack, which redirects the airflow toward the electronic modules where it is drawn again by the module fans, completing the circulation loop.

The combined airflow generated by the rack turbines and the module fans ensures that heat is efficiently transported toward the heat exchangers where it can be removed by the water cooling system. In this cooling architecture, the turbines do not directly perform the cooling function but instead maintain the airflow required for heat transport within the closed-loop system. The primary heat removal mechanism is therefore provided by the water-cooled heat exchangers.

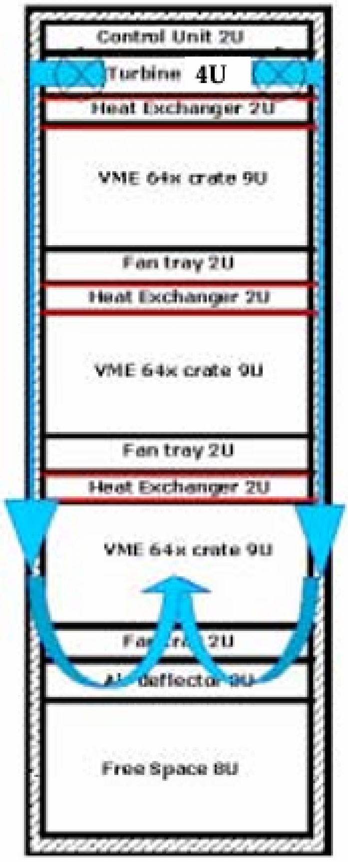

Figure 2.1: Illustration of flow within the standard rack configuration [6]

.

2.2 Background on Previous Cooling Studies

The rack cooling system was originally developed for the LEP experiments [6]. With the transition to LHC, it was necessary to evaluate whether this system could meet the cooling requirements of the new experimental environment.

A dedicated experimental study was therefore conducted using a representative rack setup to assess the performance of the system under LHC-like operating conditions. The study investigated several aspects of the cooling system, including heat exchanger performance, airflow configurations, temperature distribution within the subracks, and the possibility of operating without airflow modules.

The results demonstrated that the system is capable of dissipating up to 10 kW of power with less than 2% heat loss to the surroundings when using 2U heat exchangers. In addition, temperature levels within the subracks remained within acceptable limits, typically below 35°C. Operation without airflow modules was also found to be feasible up to approximately 5 kW [6].

2.2.1 Experimental Setup

A representative rack system was assembled in order to reproduce the expected electronics infrastructure of the LHC experiments. The rack is based on a 19-inch standard frame with a height of 56U (2.56 m) and a depth of approximately 900 mm [6].

The internal configuration consists of three repeating modules, each composed of a heat exchanger, an electronic subrack, and an airflow module. Tangential turbines are installed at the top of the rack, while an air deflector is located at the bottom to guide the airflow.

The inlet water temperature was maintained at approximately 16 °C. This value was selected in order to avoid condensation within the rack, as lowering the water temperature increases the risk of moisture formation on heat exchanger surfaces and internal components, depending on ambient temperature and relative humidity.

To simulate realistic heat dissipation, dedicated electronic load cards were developed. A total of 63 load modules were installed in the rack. These load cards allowed controlled and spatially distributed heat generation, providing a more representative thermal load compared to earlier approaches based on external resistive elements [6].

Each load card was equipped with multiple temperature sensors, enabling detailed mapping of the temperature distribution within the subracks. The sensors were calibrated in a climatic chamber and fitted using the Steinhart-Hart relation[12][6].

2.2.2 Cooling Performance Evaluation

The cooling performance of the rack was evaluated using an energy balance approach. The heat removed by the cooling water is given by:

$$P_{\text{out}} = \dot{m} c_p \Delta T \tag{2.1}$$

where $\dot{m}$ is the water mass flow rate, c_p is the specific heat capacity of water, and ΔT is the temperature difference between outlet and inlet water.

The heat loss to the environment is then calculated as:

$$P_{\text{lost}} = P_{\text{in}} - P_{\text{out}} \tag{2.2}$$

where P_{in} is the total electrical power supplied to the rack. At thermal equilibrium, this difference represents the heat released to the surrounding cavern.

2.2.3 Key Results

The study demonstrated that the cooling system can dissipate approximately 10 kW of total rack power with less than 2% heat loss to the surroundings when using 2U heat exchangers. This corresponds to a useful power dissipation of approximately 2.3 kW per subrack [6].

The temperature of the electronic modules remained within acceptable limits, typically below 40 °C, with typical values in the range of 20 °C to 35 °C, depending on the position within the rack and the local heat load distribution [6]. A comparison between 1U and 2U heat exchangers showed that the 2U configuration provides significantly better performance, with reduced heat losses and improved temperature control.

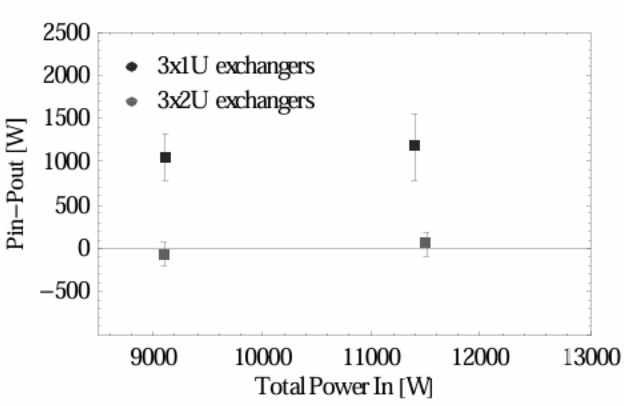

Figure 2.2: Comparison of power loss from a rack with 1U and 2U heat exchangers. [6]

2.2.4 Operation Without Airflow Modules of the Electronics

The system was also evaluated without airflow modules of the electronics inside the subracks. In this configuration, the system remained functional, but the maximum acceptable power was limited to approximately 4 kW due to local temperature increases[6].

Significant temperature non-uniformity was observed, indicating that airflow modules are essential not only for increasing airflow, but also for ensuring uniform heat distribution within the rack.

2.2.5 Effect of Cooling Water Temperature

The effect of lowering the inlet cooling water temperature from 16 °C to 14 °C was also investigated. The results showed only minor improvements in cooling performance, indicating that the system is not solely limited by water temperature, but also by airflow distribution and heat exchanger characteristics [6].

2.3 Relevance to the Present Thesis

The previous cooling study demonstrates that the closed-loop rack cooling architecture is capable of removing high thermal loads when the airflow and heat exchanger configuration are properly maintained. In particular, the results show that the system can dissipate approximately 10 kW of total rack power with minimal heat loss to the surroundings when using a configuration with 2U heat exchangers.

For the present thesis, these results provide the performance basis for the revised turbine integration. Since the heat removal capability of the rack depends strongly on internal airflow circulation, replacing the turbine system requires validation to ensure that the revised configuration can maintain an airflow performance compatible with the existing cooling concept.

Therefore, the objective of the present work is not to redesign the cooling architecture itself, but to integrate and validate a revised turbine assembly that preserves the functionality of the previously validated rack cooling system.

Chapter 3

Previous Turbine System

3.1 Tangential Turbines Cooling Concept

Tangential turbines (crossflow fans) consist of a cylindrical rotor with forward-curved blades operating within a surrounding casing and guide vane system. Air enters the rotor over a rectangular inlet section and is transported across the rotor before being discharged along its length. This configuration allows the fan to generate a distributed airflow with relatively uniform velocity over the entire width of the rotor [13].

A key characteristic of this type of fan is its ability to redirect the airflow between inlet and outlet. Depending on the casing and guide vane configuration, the discharge flow can be oriented at angles such as 90° or even 180° relative to the inlet direction [13]. Rotation could be either clock wise or counter clock wise. This makes tangential fans particularly suitable for applications where airflow must be guided within constrained geometries.

In the ATLAS rack cooling system, this capability is directly utilized. The tangential turbines as well as their casings are positioned symmetrically within the chassis. One turbine features clockwise-oriented blades, while the other is equipped with counter clockwise-oriented blades. The tangential turbines within the chassis are positioned at the top of the rack and draw heated air from the upper region of the electronic subracks. The airflow is then redirected by approximately 90° and discharged laterally into the side channels of the rack.

These side channels guide the air downward toward the bottom of the rack, where an air deflector redirects the flow back toward the electronic modules, completing the closed-loop circulation. In this configuration, the ability of the tangential fan to redirect the airflow is essential, as it enables the transition between the upward heat transport path and the downward return path. As shown in Figure 3.1, the tangential fan redirects the airflow by approximately 90°, enabling the transition from vertical intake to lateral discharge.

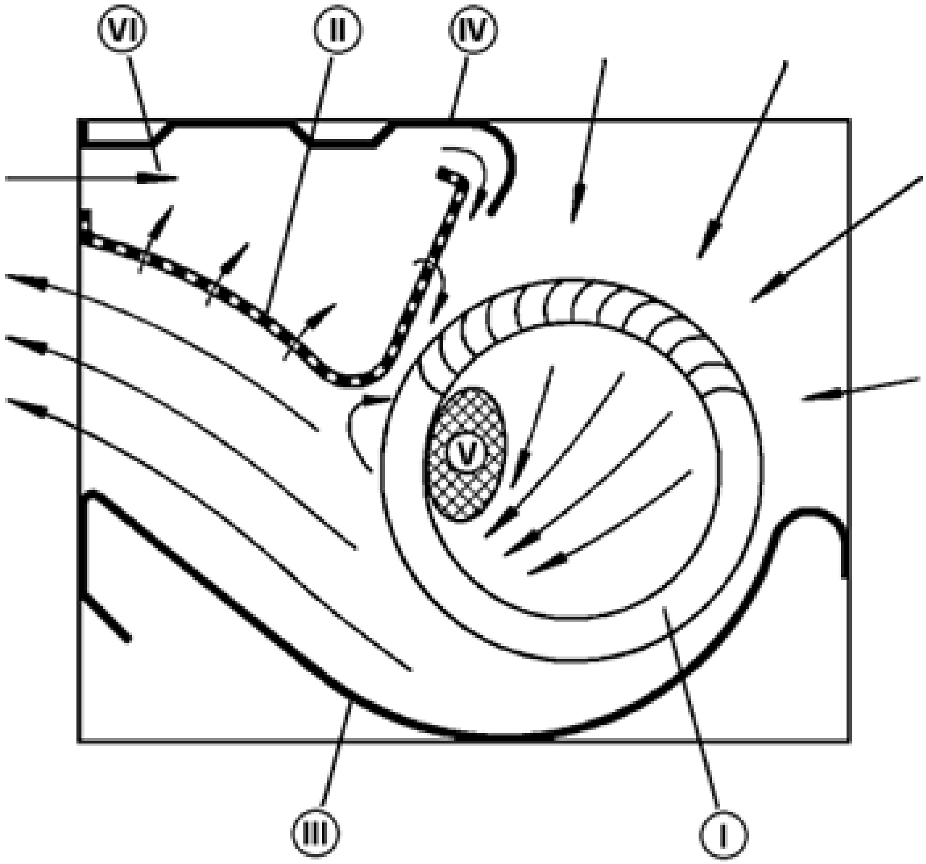

Figure 3.1: Schematic representation of the 90° airflow redirection of a tangential turbine (crossflow fan) in a casing [13].

3.2 Previous Turbine Assembly

The original turbine system used in the rack cooling infrastructure was supplied as a complete assembly by Ziehl-Abegg. Two variants of this assembly were implemented in the racks, referred to as *long* and *short* configurations.

The distinction between these configurations is based on the overall length of the chassis and the corresponding turbine:

- **Long configuration:** chassis length of 725.5 mm, equipped with a 500 mm long tangential turbine and corresponding turbine case.
- **Short configuration:** chassis length of 645.5 mm, equipped with a 420 mm long tangential turbine, corresponding turbine case with all other components remaining identical.

Apart from the difference in length, both configurations share the same mechanical concept and component architecture.

Each turbine assembly consists of two main parts:

- The **turbine kit**, which includes all rotating and functional components.
- The **chassis**, which provides structural support, positioning, and integration into the rack.

3.3 Turbine Kit

The turbine kit constitutes the functional core of the airflow generation system in the original configuration. It is responsible for driving the air circulation within the rack by converting electrical power into rotational motion and subsequently into airflow.

The turbine kit consists of a tangential turbine wheel driven by an electric (AC) motor and housed within a dedicated turbine case. Two such turbine units are integrated within each chassis, for both the long and short configurations.

The turbine wheel is enclosed within the turbine case, which defines the airflow path and provides mechanical support for the rotating components. The case also integrates several structural elements, including mounting stands and handles features, which ensure proper positioning and facilitate installation.

In addition, damping elements are incorporated between the stands and the chassis in order to reduce vibration transmission during operation. These elements contribute to the mechanical stability of the system and help limit noise and vibration effects.

The turbine system is driven by an alternating current (AC) electric motor. The motor operates at a maximum current of approximately 1.2 A and a corresponding rotational speed of approximately 2470 rpm. The input voltage is 230 V at 50 Hz, with a rated power of approximately 0.27 kW. The electric motor is mounted at the rear of the turbine and drives the turbine wheel through a direct shaft connection. Electrical connections are routed through the case to supply power to the motor.

Figures 3.2 and 3.3 illustrate the turbine kit and its main components.

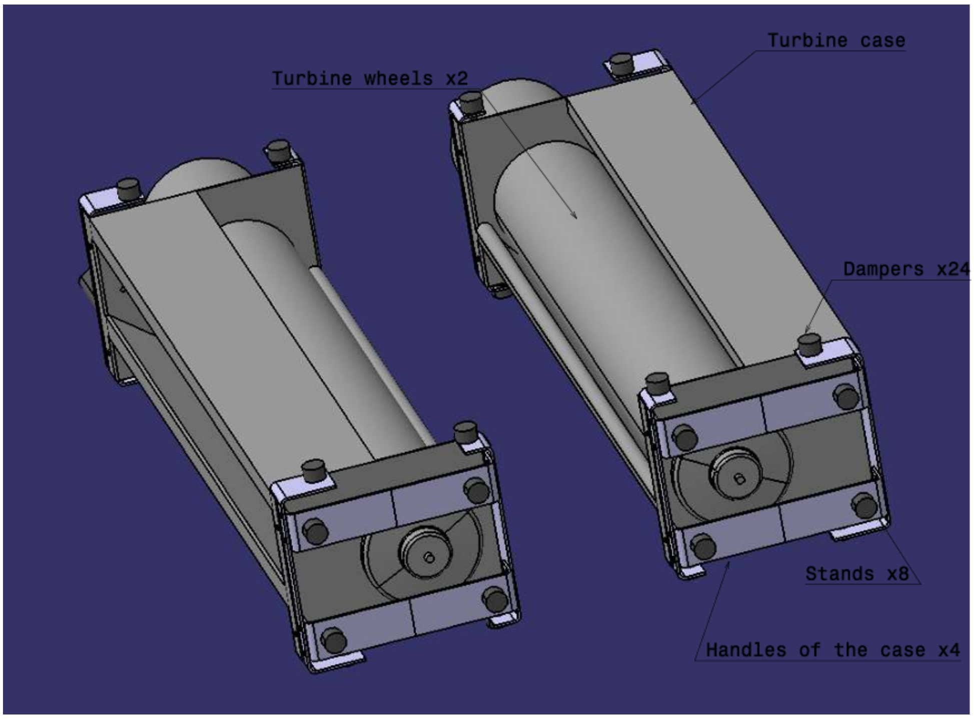

Figure 3.2: Turbine kit components including turbine case, wheels, and structural elements [4].

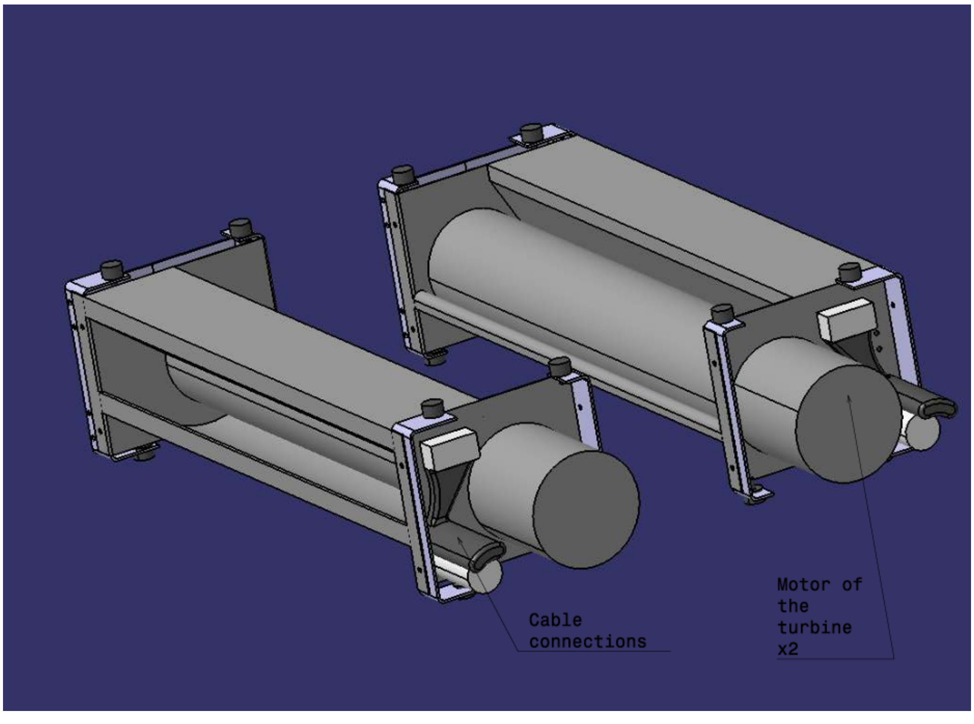

Figure 3.3: Rear view of the turbine kit showing motors and electrical connections [4].

The turbine kit's function is to ensure sufficient air circulation within the closed-loop cooling system, enabling the transport of heat from the electronic modules to the heat exchangers. Its performance is therefore essential for maintaining the effectiveness of the overall cooling architecture.

3.4 Chassis and Structural Components

The turbine chassis in the previous configuration provides the structural framework for integrating the turbine assembly into the rack. It consists of a sheet metal structure combining bent and laser-cut components, designed to support both mechanical and electrical elements of the system.

The chassis houses the turbine kit, provides mounting interfaces for the motor and turbine case, and integrates auxiliary elements such as electrical connectors and cabling. A protective shield is included to reduce the influence of the magnetic field on the motor.

The chassis also defines the positioning of the turbine within the rack and ensures proper alignment with the airflow path. Its geometry is therefore critical for both mechanical integration and cooling performance.

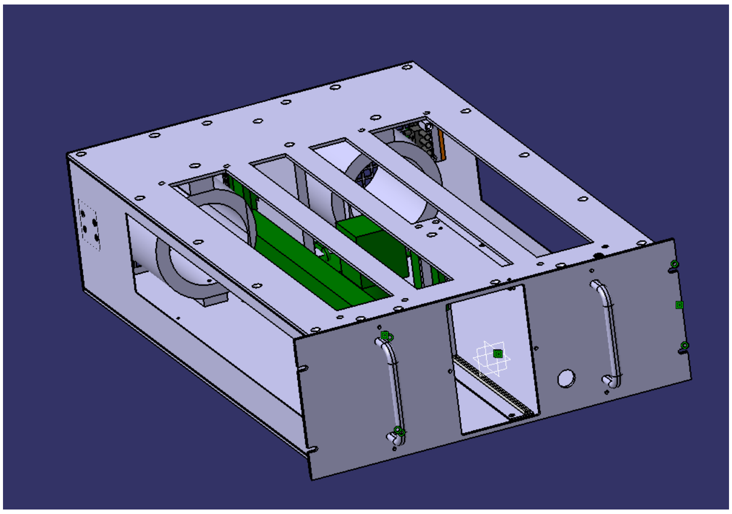

Figure 3.4: A CAD image of the chassis of the previous configuration [4].

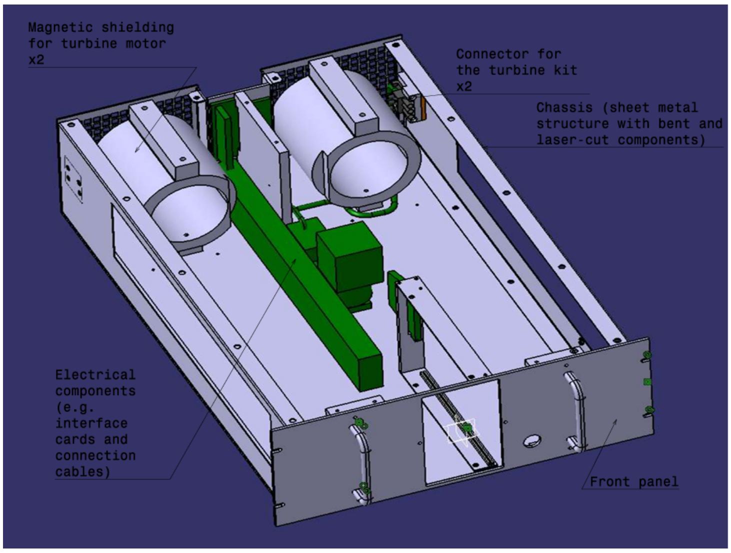

Figure 3.5: Overview of the chassis components of the previous configuration [4].

A CAD model of the previous assembly of turbine kits & chassis is provided in the annexes.

It should be noted that the available CAD models of the original configuration do not include all physical components of the turbine assembly. In particular, elements such as the rubber bearing seal, the rotor bearings, and several subcomponents of the motor and turbine are not explicitly represented, along with other minor parts.

These missing elements were identified through physical inspection of existing assemblies. A complete representation of the system, including the reconstruction of these components, is presented in Chapter 5.

Chapter 4

Motivation for the System Revision

4.1 Obsolescence of the Original Turbine

The rack cooling system described in Chapter 2 relies on tangential turbines to ensure the circulation of air within the closed-loop cooling architecture. The performance of the cooling system therefore depends strongly on the availability and reliability of these turbine units.

The turbines used in the original configuration were supplied as part of a complete turbine–chassis assembly. However since this product is no longer commercially available and considering that the plastic turbines have a limited operational lifetime of approximately five years, their replacement is required as previously mentioned in Section 1.5.

A complete redesign of the cooling system would require significant modifications to the existing rack infrastructure and would introduce considerable complexity in terms of cost, installation, and validation. For this reason, an alternative approach was adopted, consisting of selecting a replacement turbine and adapting it to the existing system.

4.2 Selection of the Replacement Turbine

The selection of a replacement turbine was constrained by the operating environment of the ATLAS detector. In particular, the presence of magnetic fields in the experimental cavern restricts the use of conventional metallic fans, requiring the use of non-magnetic materials such as plastics.

However, commercially available plastic tangential turbines are extremely limited. A market survey revealed very few viable options, and only one turbine model was identified as potentially suitable for the application. This turbine was therefore selected as the basis for the revised system.

Although the selected turbine meets the general functional requirements in terms of airflow generation, its geometry differs from that of the original turbine system.

4.3 Geometrical Differences Between the Systems

The newly selected turbine is not directly compatible with the existing mechanical configuration. Key differences were identified between the original and replacement systems:

- Differences in the interface between the motor shaft and the turbine,
- Absence of an integrated bearing seat in the new turbine,
- Rotor diameter.

These differences prevent direct installation of the new turbine into the existing assembly and require the introduction of additional components to ensure proper alignment and load transmission.

Figures 4.1–4.4 illustrate the geometrical differences between the previous and replacement turbine configurations for both long and short variants.

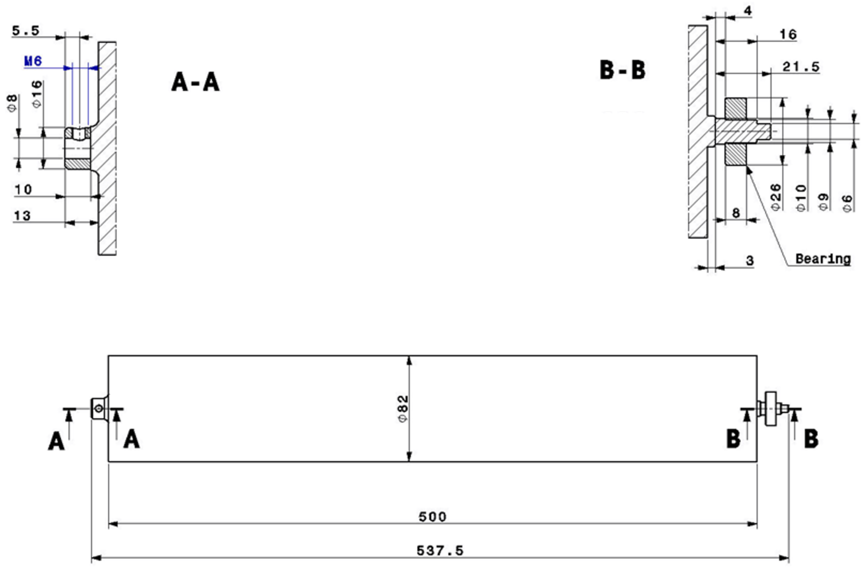

Figure 4.1: Previous turbine configuration - 500 mm [4].

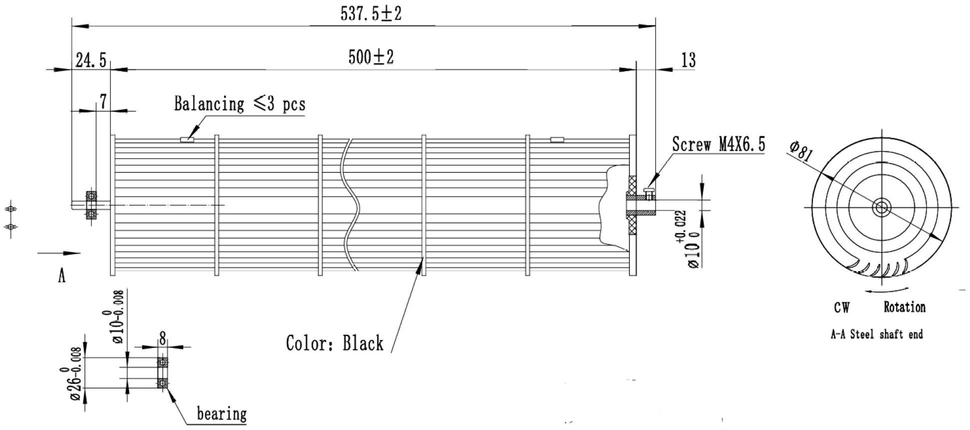

Figure 4.2: Replacement turbine configuration - 500 mm [9].

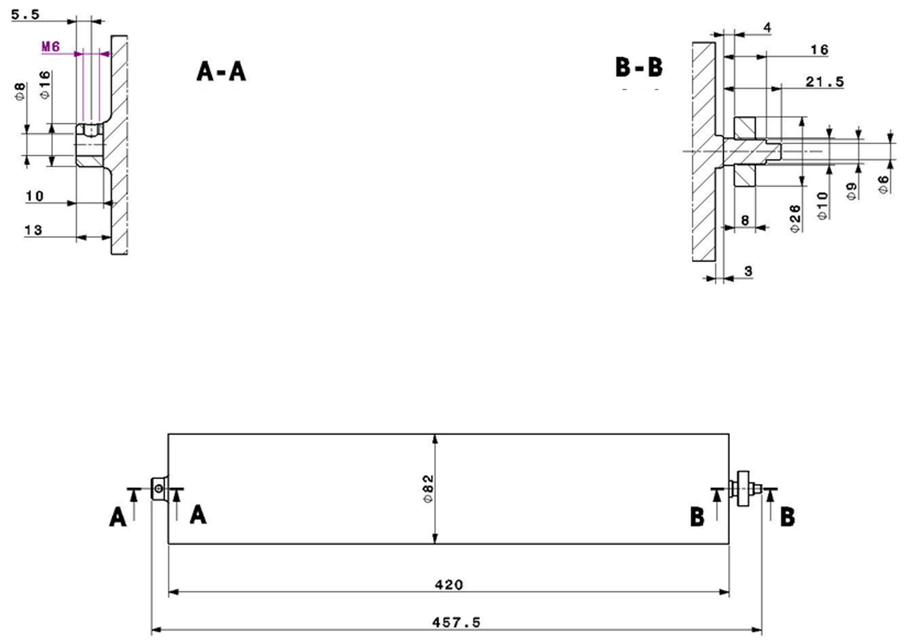

Figure 4.3: Previous turbine configuration - 420 mm [4].

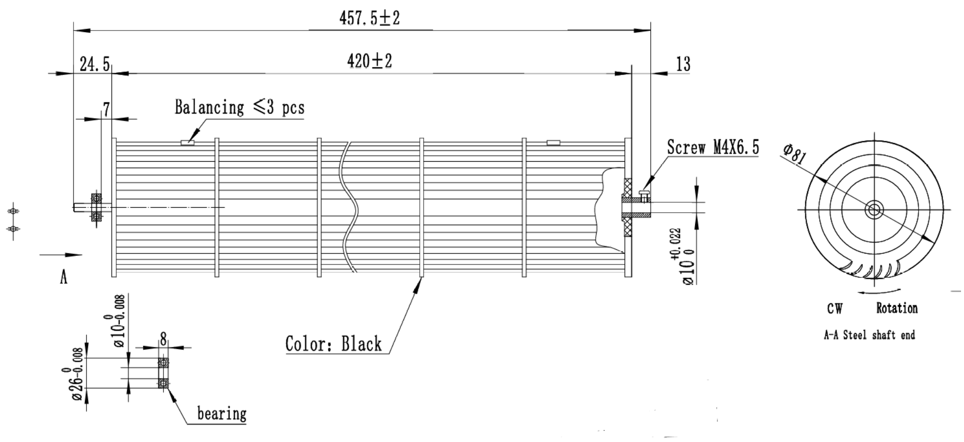

Figure 4.4: Replacement turbine configuration - 420 mm [9].

4.4 Adaptation Strategy: Spacer Components

In order to enable the integration of the selected replacement turbine into the existing system, an initial adaptation strategy based on additional spacer components was proposed.

These spacer elements were introduced to compensate for the geometrical differences between the original turbine assembly and the newly selected turbine, allowing compatibility with the existing configuration. Minor differences in rotor diameter (from 82 mm to 81 mm) were not considered critical for the integration.

Two spacer components were defined:

- A shaft spacer, intended to adapt the interface between the motor shaft and the turbine by reducing the effective diameter at the connection, thereby ensuring proper alignment and reliable torque transmission.
- A bearing spacer, intended to recreate the bearing seat functionality that was originally integrated into the previous turbine design, ensuring correct axial positioning and support of the bearing.

These components form the basis of the revised turbine integration concept.

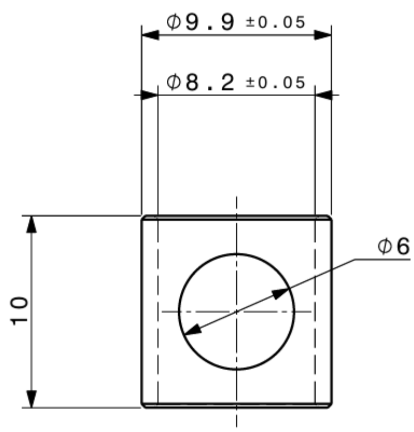

Figure 4.5: Shaft spacer component - Spacer 1 [4].

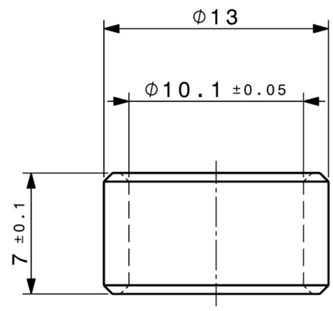

Figure 4.6: Bearing spacer component - Spacer 2 [4].

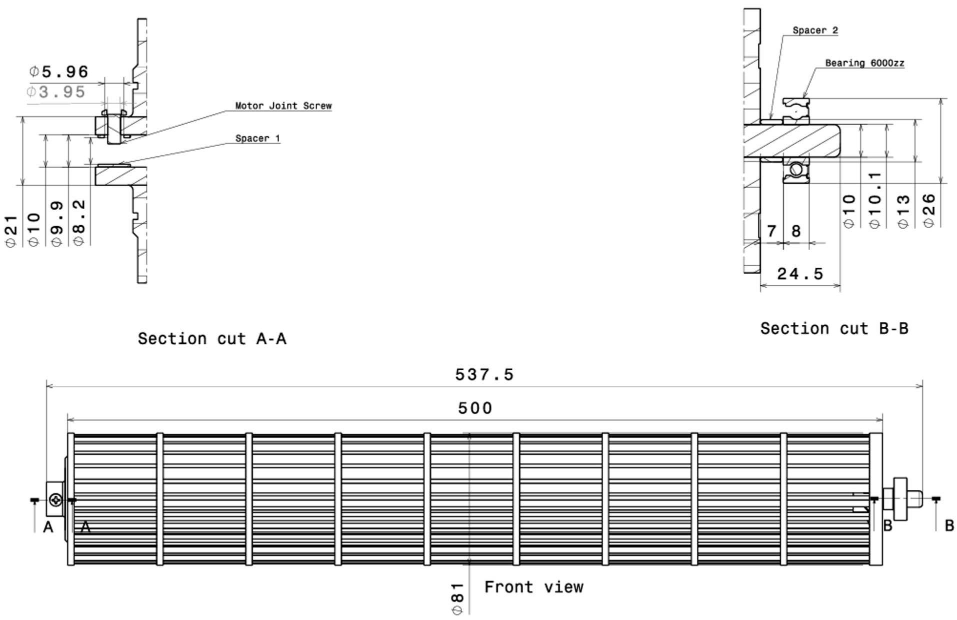

Figure 4.7: Spacer integrated revised turbine configuration - 500 mm

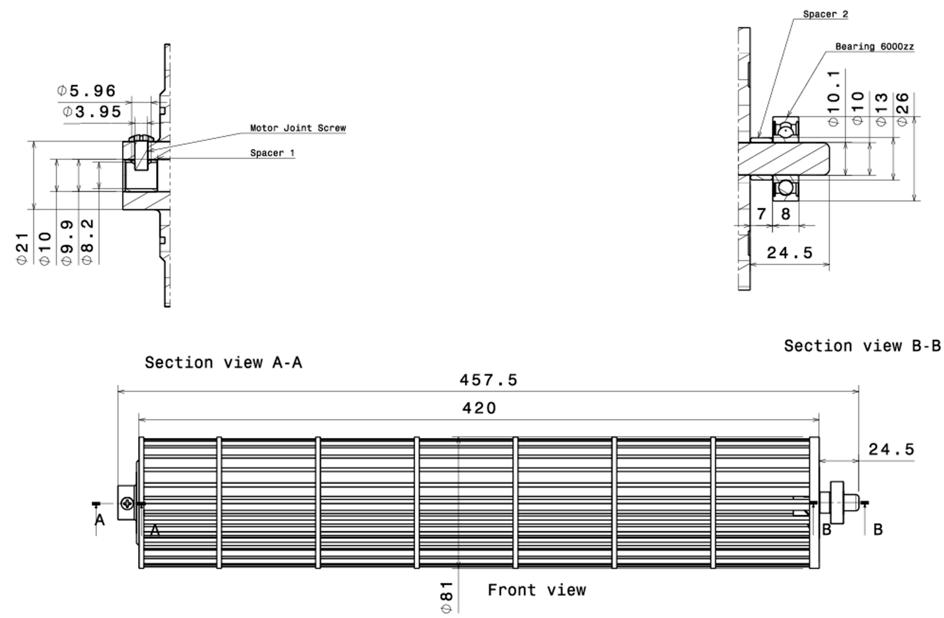

Figure 4.8: Spacer integrated revised turbine configuration - 420 mm

Even though spacer elements provided a foundation for the integration of the revised system; further integration activities should be carried out for final validation, aspects such as preload conditions, tolerance effects, functionality and the structural integrity of the system must be carefully evaluated to ensure reliable operation. These aspects are addressed in the following chapters.

Chapter 5

CAD Reconstruction and Reverse Engineering

5.1 Reconstruction Methodology

The integration of the revised turbine system required the creation of a complete and consistent CAD representation of the assembly. Since a fully defined digital model of the system was not available, a reconstruction process combining existing documentation, supplier data, and reverse engineering was carried out.

For the turbine chassis, CAD models were obtained directly from the manufacturer (Rack Peruzzi). These models included the main structural components and sheet metal parts of both long and short configurations. Minor updates were implemented based on physical inspection of the available hardware,

The turbine case was partially available through internal CERN CAD models. However, these models did not fully reflect the current physical components. Therefore, additional modifications were introduced based on direct measurements and comparison with the existing assemblies in order to ensure geometric consistency, including adjustments to hole positions and the addition of missing features required for integration.

The newly selected turbine did not have a complete 3D CAD model available. Supplier documentation provided only limited two-dimensional drawings. As a result, the turbine geometry was reconstructed using a combination of available drawings and reverse engineering based on physical measurements of the component.

Similarly, the electric motor and its subcomponents, including elements such as the shaft, bearings, and auxiliary parts, were not available as complete CAD models. These components were therefore reconstructed entirely through reverse engineering, using caliper measurements and visual inspection of the physical assembly.

This combined approach ensured that all components required for the integration study were represented within a coherent CAD environment, enabling further assembly and analysis work.

5.2 Reconstructed Components and CAD Models

Based on the methodology described above, a complete set of CAD models was developed for the turbine assembly and its integration within the chassis.

The reconstructed system includes the following components:

- Chassis,
- Turbine kit,
- Electric (AC) motor and its subcomponents,

Each component was modeled with sufficient geometric detail to ensure correct assembly positioning and interface definition. Particular attention was given to critical interfaces such as the motor–turbine connection and the bearing support regions.

The resulting CAD models allow visualization of the complete assembly and provide the basis for the integration of the revised turbine system. Representative views of the reconstructed components are presented in the following figures. For the chassis and the turbine kit, the short configuration is shown in the following figures, while the CAD models of both long and short configurations are provided in the annexes.

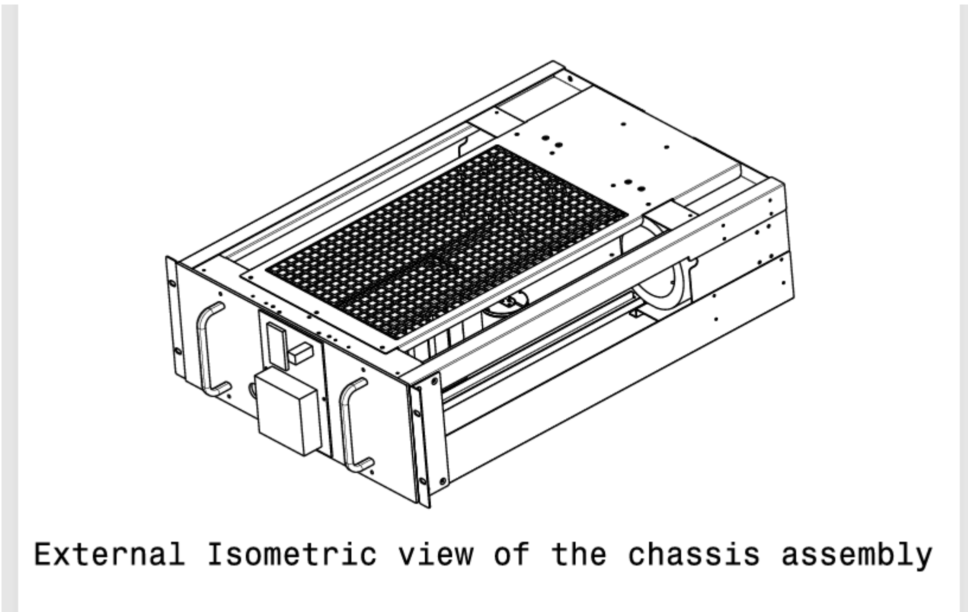

Figure 5.1: External Isometric View of the Chassis Assembly - 645.5 mm in length

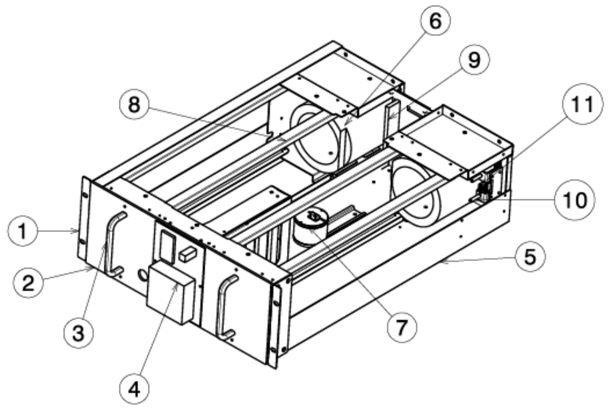

Internal isometric view of the chassis assembly

Chassis BOM (critical components only)		
No.	Name	Qty.
1	Rack installation panel	2
2	Front panel	1
3	Chassis handle	2
4	Monitoring card (MON Card)	1
5	Chassis (including sub-panels)	1
6	Shielding for the motor	2
7	Shielding for the Aux card	1
8	Rails for the turbine kit	8
9	Back card	1
10	Alignment pins for the turbine kit	4
11	Wieland female electrical connector	2

Figure 5.2: Internal isometric view of the chassis assembly with identification of the main components - 645.5 mm in length. Only components relevant to the turbine integration are shown.

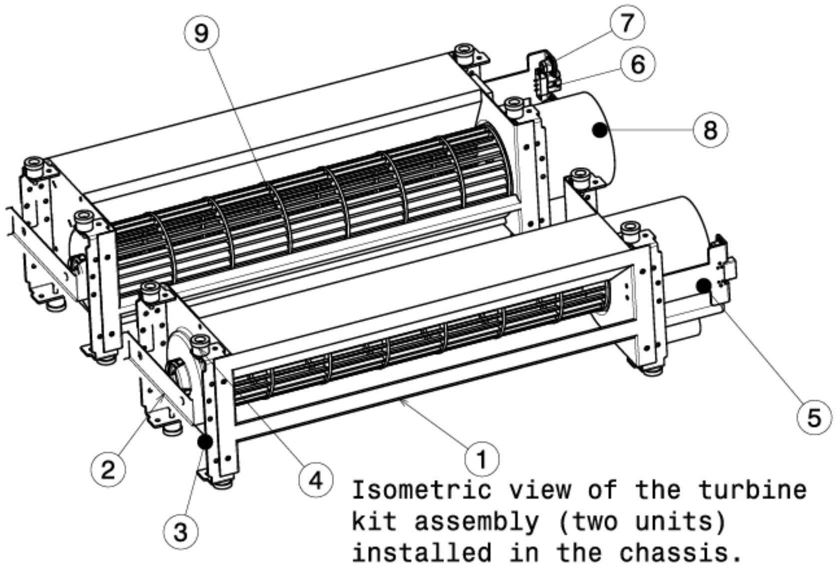

BOM for the turbine kit assembly of one chassis (excluding turbine & casing joining components)		
No:	Name:	Qty.:
1	Case of the turbines	2
2	Handle of the case	2
3	Stands	8
4	Vibration dampers	16
5	Mounting plate for Wieland male connector	2
6	Wieland male electrical connector	2
7	Bushing for alignment pins	4
8	Electric motor	2
9	Tangential turbine wheel	2

Figure 5.3: Isometric view of the turbine kit assembly (two units) integrated within the chassis - 645.5 mm in length, with identification of the main components, excluding turbine-case-motor joining components.

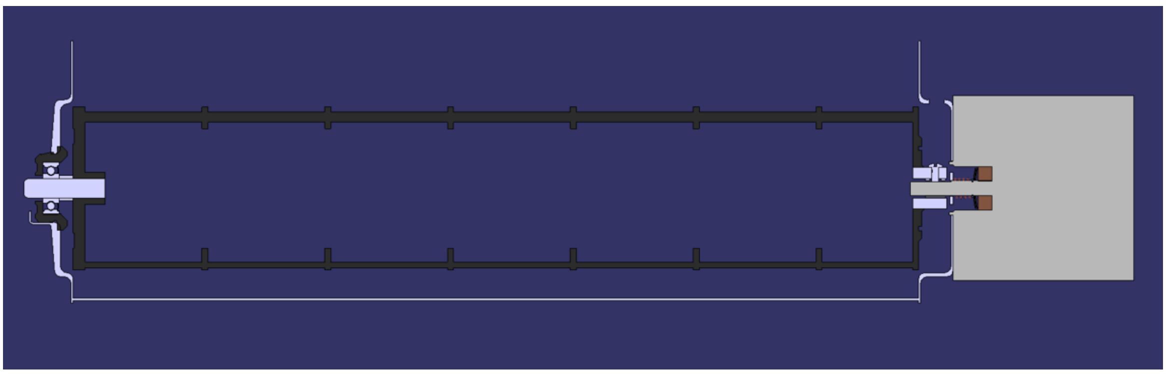

Figure 5.4: Section view of the turbine wheel, casing and motor assembly

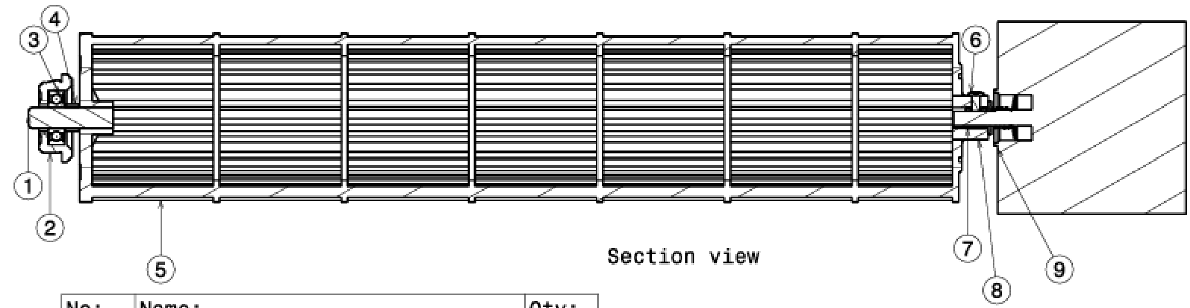

No:	Name:	Qty:
1	Turbine shaft	1
2	Bearing seal	1
3	6000zz bearing	1
4	Turbine spacer 2	1
5	Plastic turbine	1
6	Turbine motor joining screw	1
7	Turbine spacer 1	1
8	Turbine & motor junction piece	1
9	Motor assembly	1

Figure 5.5: BOM of the turbine wheel and motor assembly, illustrating the axial arrangement and interfaces between the turbine, spacers, bearing, rubber sealing element, and motor assembly.

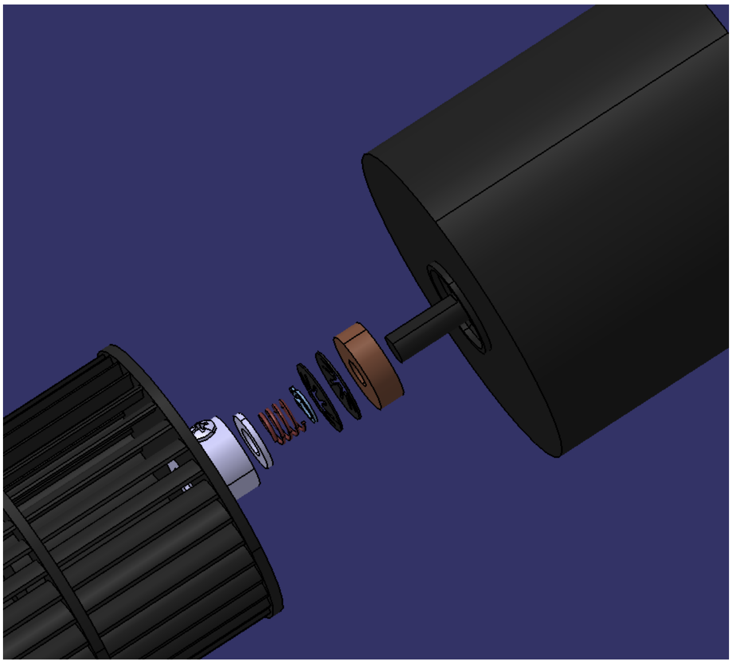

Figure 5.6: Exploded view of the turbine–motor interface

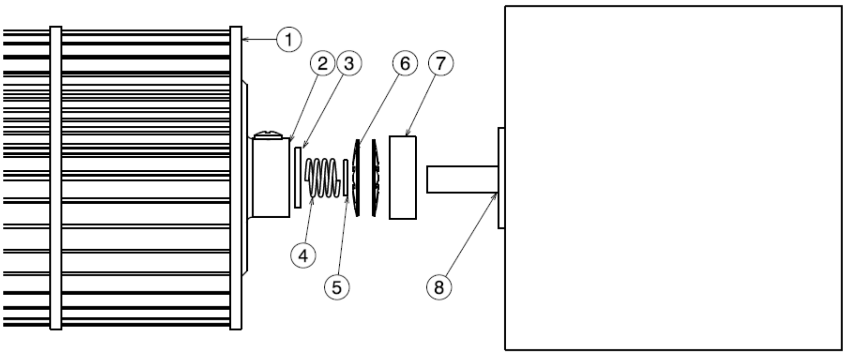

No:	Name:	Qty.:
1	Plastic turbine	1
2	Turbine & motor junction piece	1
3	Flat washer	1
4	Compression spring	1
5	Circlip	1
6	Starlock washer	2
7	608zz bearing	1
8	Motor	1

Figure 5.7: BOM of the turbine–motor interface

Note: Figure 5.7 represents the reconstructed assembly used to analyse axial preload and component interaction.

The reconstructed CAD models provide a consistent and complete geometric representation of the turbine system and its integration within the chassis. The level of detail achieved is sufficient to define all critical interfaces and to ensure correct assembly positioning of the components.

Through the reconstruction process, particular attention was given to the turbine–motor interface and the bearing support regions, as these areas are directly related to the mechanical integrity and operational reliability of the system. The resulting models therefore serve not only as a visualization tool, but also as a basis for identifying potential integration issues. In this context, the reconstructed assembly revealed some challenges, particularly related to axial positioning and component interaction at the turbine–motor interface. These observations form the starting point for the analysis presented in the following chapter.

Additionally, the CAD models developed during the project are provided in the Appendix files. Depending on their intended purpose, different levels of geometric detail were adopted for analysis models and assembly models.

5.3 Materials

Due to the magnetic field in ATLAS's experimental cavern, all metallic parts of the chassis and the turbine kit are made out of non-magnetic metal, either aluminium or stainless-steel. To ensure corrosion resistance and surface protection, appropriate treatments are also applied depending on the material, such as passivation for stainless steel and conversion coatings (e.g. Alodine 1200 or equivalent) for aluminium components. The tangential turbine wheels are manufactured from a polymer material (AS) reinforced with approximately 30% glass fiber. This non-metallic material was selected to prevent interaction with the magnetic field. In addition, the use of this material is consistent with commercially available solutions, as it is employed by the selected turbine supplier.

Chapter 6

Integration Challenges and Axial Positioning Analysis

A challenge for the integration was identified in the axial positioning system. The new turbine introduces a tolerance range of approximately ± 2 mm, which, according to the CAD models, exceeds the capability of the original spring to maintain consistent contact within the assembly.

A critical element of the system is the rubber bearing seal, which serves multiple functions. It acts as a compliant bearing support, provides vibration damping, and contributes to axial positioning of the rotating assembly.

Observations of the original system showed that the turbine's bearing (6000ZZ), was not always fully seated within the bearing seal. Despite this, the system operated successfully over its expected lifetime. This suggests that the design tolerates a certain degree of positional variation, likely due to the compliant nature of the rubber interface.

However, in order to develop a more robust and reproducible solution, a redesign of the spring component is evaluated. This involved determining appropriate spring characteristics to ensure contact throughout the tolerance range of the turbines and to provide sufficient preload across the entire tolerance range while avoiding excessive loading of the bearings.

The axial arrangement of the relevant components is previously shown in Figure 5.5.

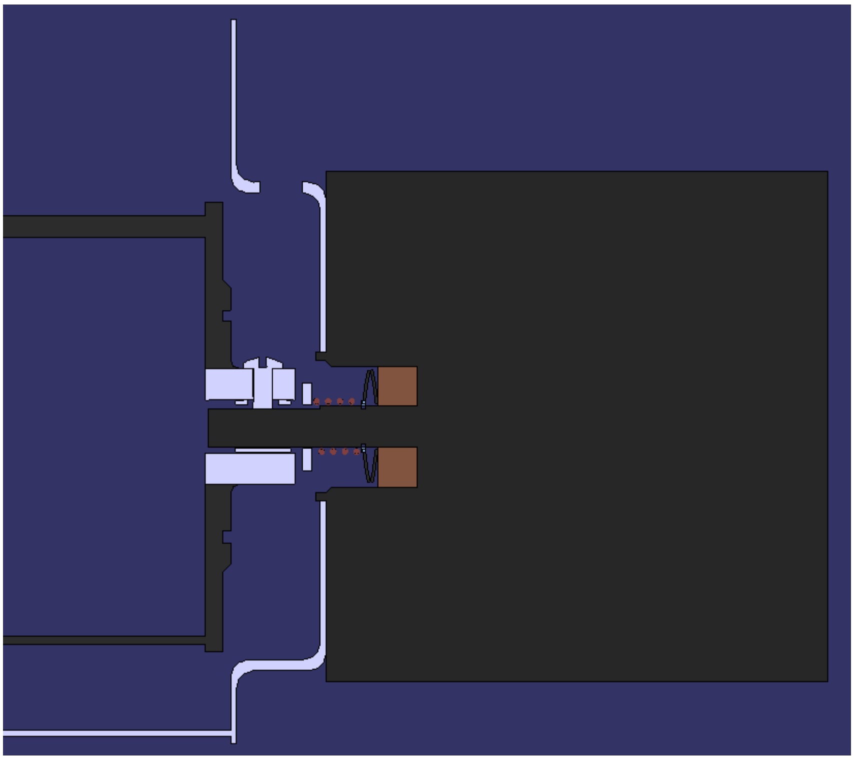

Figure 6.1: Section view of the turbine–motor interface illustrating the gap between motor junction piece and the flat washer. The corresponding bill of materials (BOM) for the shown components is previously provided in Figure 5.7.

6.1 Analysis

The following analysis is performed on the short (420 mm) turbine configuration. However, the same reasoning is applicable to the long (500 mm) configuration, as the relative tolerance stack and the axial positioning concept remain identical.

The non-contact condition identified in the CAD model was first verified using a simplified physical prototype with the 500 mm turbine configuration, confirming that the observed gap is representative of the real system. Following this validation, the tolerance ranges of the relevant components were defined. This step allows quantification of the axial variation within the assembly and its influence on contact conditions and preload generation.

The components contributing to the axial positioning of the turbine–motor assembly and their respective tolerance ranges were defined as follows:

- **Turbine length**: ±2 mm (dominant contribution; based on supplier specifications)
- **Bearings (6000ZZ / 608ZZ)**: approximately −0.12 mm (manufacturing tolerance from bearing specifications)
- **Turbine spacer 2**: ±0.1 mm (based on validated 2D drawings of the component)

- **Turbine–motor junction piece**: ±0.1 mm (assumed, as no tolerance data was provided by the supplier)
- **Turbine casing**: ±0.1 mm (assumed, as no tolerance data was provided by the supplier)
- **Bearing seal (rubber)**: not defined as a fixed tolerance (treated as a compliant element capable of accommodating axial variation)

Based on the defined tolerance ranges, it was observed that the components located on the opposite side of the motor (i.e. 6000ZZ bearing, turbine spacer 2, and the bearing seal) exhibit relatively small dimensional variations compared to the turbine length tolerance. Therefore, it is assumed that the dominant axial variation introduced by the turbine is primarily accommodated on the motor side of the assembly.

6.1.1 Axial Gap Evaluation

The axial gap between the turbine and the spring interface was evaluated across the tolerance range of the turbine.

At the lower tolerance limit (i.e. 418 mm), a gap of approximately 2 mm is observed between the flat washer and the turbine–motor junction component, resulting in no contact with the spring.

At nominal conditions, the turbine is in near contact with the washer, but no spring compression.

At the upper tolerance limit (i.e. 422 mm), the spring is compressed by approximately 2 mm.

These observations are illustrated in Figures 6.2, 6.3, and 6.4.

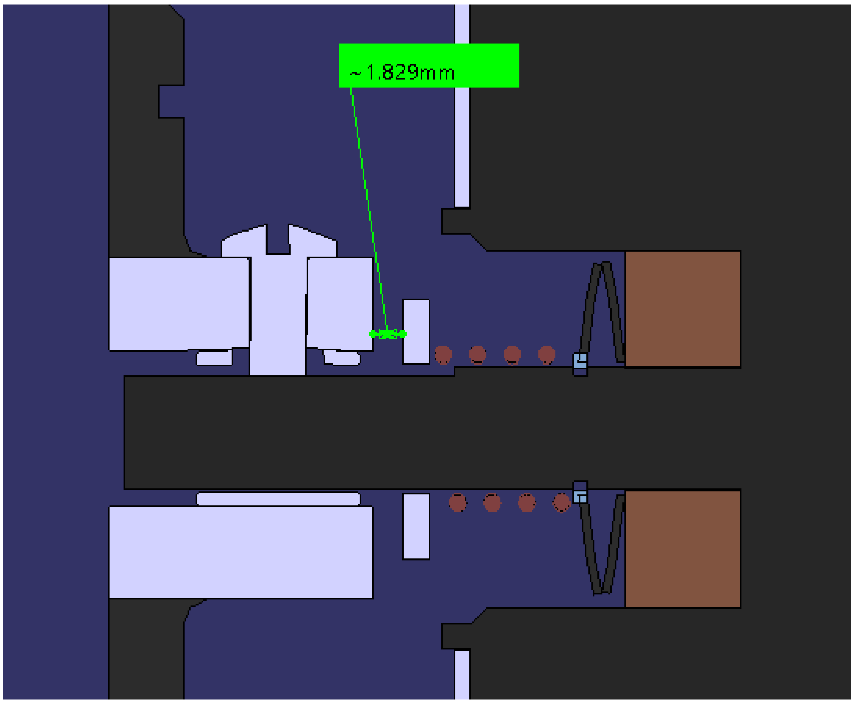

Figure 6.2: Axial configuration at the lower tolerance limit of the turbine length (418 mm), showing the presence of a gap between the flat washer and the turbine–motor junction component, resulting in no contact with the spring.

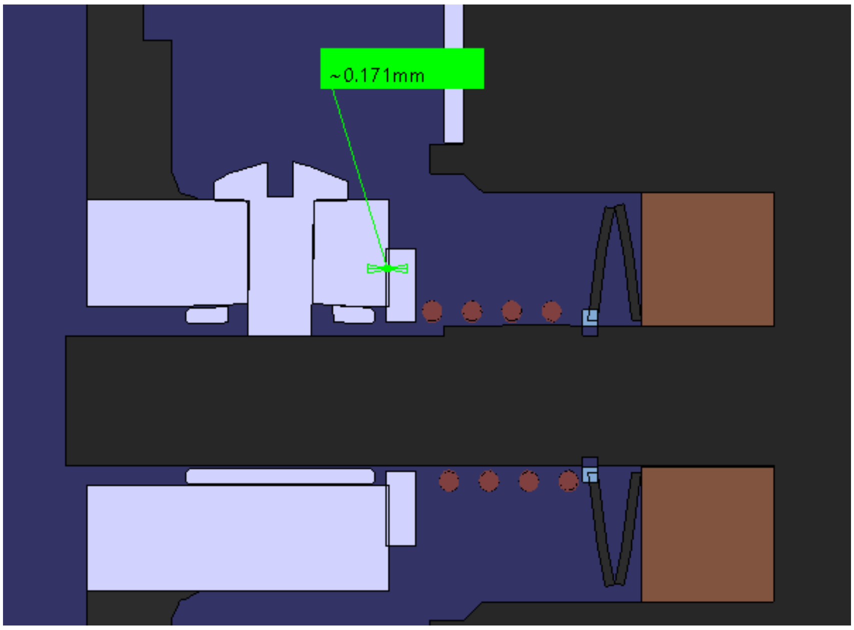

Figure 6.3: Axial configuration at nominal turbine length (420 mm), showing initial contact between the flat washer and the turbine–motor junction component, with no spring compression and no effective preload generation.

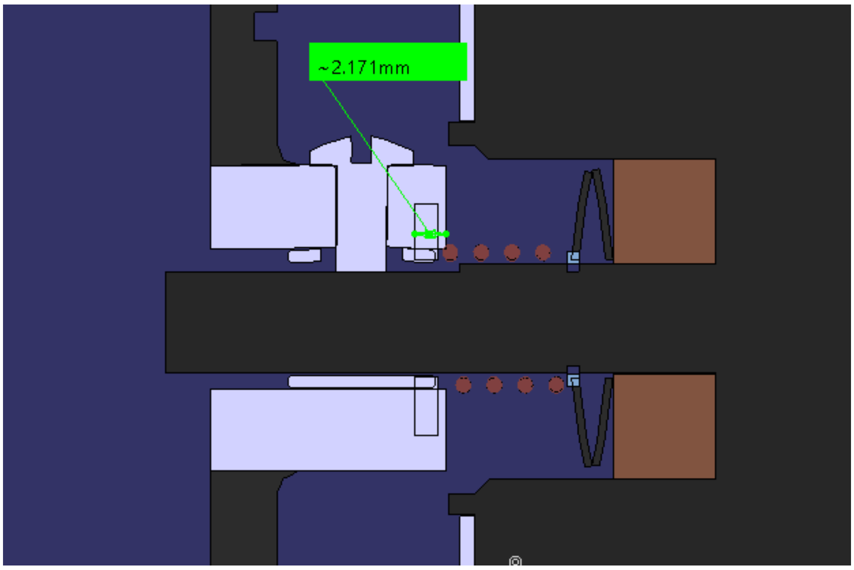

Figure 6.4: Axial configuration at the upper tolerance limit of the turbine length (e.g. 422 mm), showing approximately 2 mm compression of the spring and resulting preload within the assembly.

The observed variation in axial positioning directly affects the functionality of the spring. At the lower tolerance limit, the absence of contact results in no preload generation, while at nominal conditions only minimal contact is achieved. At the upper tolerance limit, the spring is compressed, resulting in a preload force. This behavior indicates that the current spring is not capable of ensuring continuous contact across the full tolerance range, leading to inconsistent preload conditions within the assembly.

Based on the geometrical parameters of the previously used spring, the spring stiffness was estimated assuming a shear modulus of $G = 79{,}300\ \mathrm{N/mm^2}$. The resulting stiffness is approximately $k \approx 6.4\ \mathrm{N/mm}$. Under maximum compression conditions (~ 2 mm), the corresponding preload force is estimated as $F = kx \approx 12.8$ N.

$$
\begin{aligned}
\text{Free length:} \quad & L_0 = 9.3\,\mathrm{mm} \\
\text{Wire diameter:} \quad & d = 1\,\mathrm{mm} \\
\text{Outer diameter:} \quad & D_o = 10.2\,\mathrm{mm} \\
\text{Total number of coils:} \quad & n_t = 4 \\
\text{Active coils:} \quad & n \approx 2 \\
\text{Shear modulus:} \quad & G \approx 79{,}300\,\mathrm{N/mm^2} \\
\text{Spring stiffness:} \quad & k \approx 6.4\,\mathrm{N/mm}
\end{aligned}
$$

6.1.2 Evaluation of Possible Solutions

Based on the identified gap and the resulting lack of consistent spring engagement, two primary modification strategies were considered:

- Increasing the thickness of the flat washer
- Selecting a spring with modified characteristics (e.g. increased free length)

In order to ensure that the spring is engaged even at the lowest end of the turbine tolerance, a minimum compression of approximately 1 mm is required. Based on the estimated spring stiffness ($k \approx 6.4$ N/mm), this corresponds to a preload force of approximately 6.4 N. To achieve this condition, the washer thickness would need to be increased to approximately 4.6 mm. However, this modification leads to unfavorable behavior at the upper tolerance limit. At the maximum turbine length, the spring would be compressed by approximately 5 mm, resulting in an estimated preload force of about 32 N. Such compression approaches the solid height of the spring. Considering the initial free length ($L_0 = 9.3$ mm) and wire diameter ($d = 1$ mm), the remaining length under compression would be approximately 4.3 mm, which is close to the solid length. This condition is undesirable, as it may lead to excessive stresses, reduced spring life, and potential loss of elastic behavior. Therefore, increasing the washer thickness is not considered a viable solution.

Consequently, the solution became the redesign of the spring element to accommodate the full tolerance range while maintaining controlled preload levels.

6.2 Spring Selection Methodology

The spring selection was guided by the following requirements:

- Ensure continuous contact across the entire turbine tolerance range
- Avoid excessive preload that could negatively affect bearing performance
- Maintain relatively stable preload variation within the tolerance range

6.2.1 Dimensional Selection Logic

The spring must satisfy a set of geometric and assembly-related constraints in order to function correctly within the system. These constraints ensure that contact is maintained across the full tolerance range while avoiding mechanical interference or excessive deformation.

Accordingly, the spring must satisfy the following conditions:

- The free length must exceed the maximum gap in order to ensure contact across the full tolerance range

- The compressed length must remain above the minimum allowable height to avoid approaching solid conditions

- The inner diameter must ensure proper fitting and alignment on the motor shaft

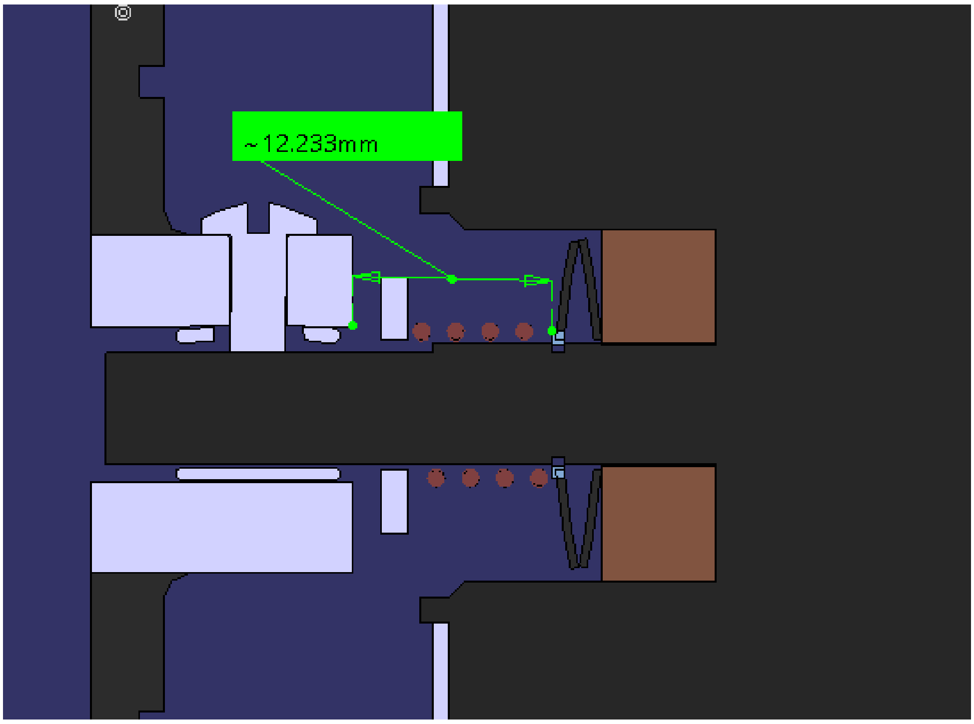

Figure 6.5: Maximum gap between the circlip and the turbine–motor junction piece at the lowest turbine tolerance condition, used as a reference for defining the minimum required free length of the spring.

Therefore, the dimensional constraints of the spring are defined as follows:

- Minimum allowable compressed height: ≤ 7.5 mm (at maximum turbine length)

- Inner diameter: 8.1–8.5 mm (to fit the motor shaft)

- Minimum free length: ≥ 13 mm (to ensure contact at minimum turbine length)

6.2.2 Target Preload Selection

For defining the target preload range, manufacturer guidelines and literature on rolling bearing applications are thoroughly studied. According to these sources, preload can improve system stiffness, guidance, and noise behavior [11]. However, excessive preload leads to increased friction, heat generation, and reduced bearing lifetime [2].

Furthermore, it is emphasized that preload values determined analytically during the design phase should be validated experimentally [2], as it is difficult to capture all influencing factors through simplified calculations alone.

In order to ensure that the proposed preload values remain within acceptable limits, a check of the maximum allowable axial load for the bearings (6000ZZ and 608ZZ) was performed.

According to SKF rolling bearing specifications, the allowable axial load for deep groove ball bearings can be approximated as:

- $F_a \leq 0.5\, C_0$ (general condition) [11]
- For small or light series bearings: $F_a \leq 0.25\, C_0$ [11]

Using a conservative approach and considering the 608ZZ bearing as the limiting case, the allowable axial load is estimated as:

$$F_a \leq 0.25 \cdot C_0 = 0.25 \cdot 1370 \approx 342.5 \text{ N}$$

This value is significantly higher than the preload forces required for axial positioning in the present application. Therefore, the bearing load capacity is not a limiting factor in the spring design.

Further guidance from the SKF catalogue provides an estimation for preload forces in small electric motor applications, expressed as:

$$F = k \cdot d \text{ [11]}$$

where F is the preload force, k is a factor depending on application conditions, and d is the bearing bore diameter [11].

For small electric motors, a minimum value of $k = 0.005$ is recommended [11]. Using the 608ZZ bearing (with $d = 8$ mm), the estimated preload is:

$$F = 0.005 \cdot 8 = 0.04 \text{ kN} = 40 \text{ N}$$

This value is considered as a theoretical upper reference for preload selection in the present system.

Potential Critical Interfaces

A potentially critical interface in the assembly is the contact between the "Turbine Spacer 2" and the plastic turbine. This interface is directly subjected to the axial preload force.

To evaluate its load-bearing capability, a conservative analysis was performed. Based on the nominal contact area and material properties of the AS 30% glass-fiber reinforced, the allowable stress was reduced to account for long-term operation.

- **Nominal contact area:**

$$A = 52.6\,\mathrm{mm}^2$$

- **Material allowable stress:**

$$\sigma_{\mathrm{max}} = 115\,\mathrm{MPa}$$

Conservative assumptions:

- Effective contact area reduced by 50%:

$$A_{\mathrm{eff}} = 26.3\,\mathrm{mm}^2$$

- Allowable stress reduced to 20%:

$$\sigma_{\mathrm{allow}} = 23\,\mathrm{MPa}$$

Maximum allowable force:

$$F_{\mathrm{max}} = \sigma_{\mathrm{allow}} \cdot A_{\mathrm{eff}} = 23 \times 26.3 \approx 605\,\mathrm{N}$$

Even under conservative assumptions (reduced effective contact area and allowable stress), the resulting maximum allowable force was found to be significantly higher than the expected preload forces.

Therefore, this interface is not considered a limiting factor in the design.

Selected Preload Range

Based on the analytical estimation of the existing spring and the defined geometric constraints, a preload range of approximately 6.4 N to 20.3 N was identified, with a target mean value of approximately 14 N. Which can be computed as follows:

$$\begin{aligned}
\text{Free length:}\quad & L_0 = 9.3\,\mathrm{mm} \\
\text{Solid length:}\quad & L_s = 4\,\mathrm{mm} \\
\text{Working range:}\quad & \Delta L = L_0 - L_s = 5.3\,\mathrm{mm} \\
\text{Safe operation} & \\
\text{(assumed as 60\% of the working range):}\quad & \Delta L_{\text{safe}} = 3.18\,\mathrm{mm} \\
\text{Minimum compression:}\quad & x_{\min} = 1\,\mathrm{mm} \\
\text{Maximum compression:}\quad & x_{\max} = 3.18\,\mathrm{mm} \\
\text{Preload force range:}\quad & F = kx \Rightarrow 6.4 \leq F \leq 20.3\,\mathrm{N} \\
\text{Mean preload:}\quad & F_{\text{mean}} \approx 14\,\mathrm{N}
\end{aligned}$$

This value provides sufficient contact and positioning capability without introducing excessive loading on the bearings.

Considering that the turbine system is designed for a finite operational lifetime (approximately 5 years), this preload level was selected as a practical and robust design solution.

Chapter 7

Technical Specification Preparation and Procurement Strategy

In parallel with the mechanical integration and validation activities, a procurement and configuration strategy was developed in order to support the large-scale preparation of the upgraded turbine chassis assemblies.

The objective was to maximize the use of the existing inventory while minimizing the number of 'to be procured' components and maintaining compatibility with the operational requirements of the rack system.

7.1 Bill of Materials Development

A complete bill of materials (BOM) was first prepared for a fully assembled turbine chassis including the tangential fans, motor interfaces, fastening elements, and structural subcomponents.

The BOM was used as the basis for inventory tracking, procurement planning, and estimation of the number of assemblies that could be build using the available stock.

7.2 Inventory Assessment

An inventory assessment was subsequently performed for all available chassis and subcomponents. Existing stock included both short and long chassis configurations, as well as partially assembled units and reusable components recovered from previous systems.

The assessment identified the quantities of immediately available assemblies and the components requiring procurement in order to achieve the target number of the required ventilation systems.

7.3 Definition of Required Chassis Quantities

The target quantity for the integration campaign was defined as 82 turbine chassis assemblies.

Since the electronics installed inside the racks are shorter than both the short and long chassis configurations, both configurations are functionally compatible with the application. Therefore, the distribution between short and long chassis was optimized primarily from an inventory and procurement perspective rather than from a functional constraint.

7.4 Configuration Selection Strategy

To maximize the use of the available inventory, limiting components within the stock were identified and used to define the final configuration distribution.

The analysis showed that the available inventory contained:

- 68 short empty chassis
- 2 long empty chassis
- 67 short turbine case
- 71 long turbine case

Based on these constraints, the selected configuration strategy consisted of:

- 67 short chassis assemblies
- 15 long chassis assemblies

This distribution minimized the procurement requirements by maximizing reuse of the available short chassis inventory.

7.5 Procurement Optimization

Based on the selected configuration strategy, procurement activities were limited primarily to:

- Subcomponents related to the motor integration
- Plastic turbine wheels
- 13 additional long empty chassis

This approach significantly reduced manufacturing scope, procurement cost, and lead time compared to complete production of new assemblies.

The resulting procurement strategy enabled efficient utilization of the existing stock while ensuring compatibility with the upgraded turbine system.

7.6 Preparation of the Technical Specification for the Long Empty Chassis

Following the definition of the procurement quantities, a technical specification was prepared for the manufacturing and procurement of the long empty chassis assembly.

The objective of the specification was to ensure dimensional compatibility with the existing rack infrastructure while allowing integration of the revised turbine system. The specification package included:

- 3D CAD model of the long empty chassis (Annex A).
- 2D technical drawings of the critical dimensions for turbine & case assembly integration (Annex B).
- 3D Model of the chassis, assembled with turbine & case assemblies for reference (Annex C).
- Technical specification

Particular attention was given to defining the critical dimensions associated with the turbine positioning, guide interfaces, and mounting locations, as these directly influence assembly compatibility and alignment within the rack system.

The specification package is provided in the Annexes.

Chapter 8

Simplified Rotor Dynamic Analysis

8.1 Objective

Prior to prototype testing, a simplified rotor dynamic analysis was performed in order to evaluate whether the revised turbine assembly could operate close to a structural resonance condition.

The objective of the analysis was not to develop a complete rotor dynamic model of the system, but rather to estimate the first bending natural frequency of the turbine assembly and compare it with the operating frequency range of the motor.

Since the 500 mm turbine represents the longest and therefore most flexible turbine configuration used in the cooling system, the analysis was performed on this assembly. The shorter 420 mm turbine is expected to exhibit higher natural frequencies and was therefore considered less critical from a rotor-dynamic perspective.

8.2 Rotor Model

The turbine was represented using a simplified beam-based rotor model. The plastic turbine body was discretized into a series of lumped masses connected by Euler-Bernoulli beam elements. The lumped masses were positioned at the wheel sections and represented the combined mass of the plastic wheel segments, the bearings, the spacers and the steel shafts at the relevant nodes.

Figure 8.1 presents the turbine assembly considered in the analysis.

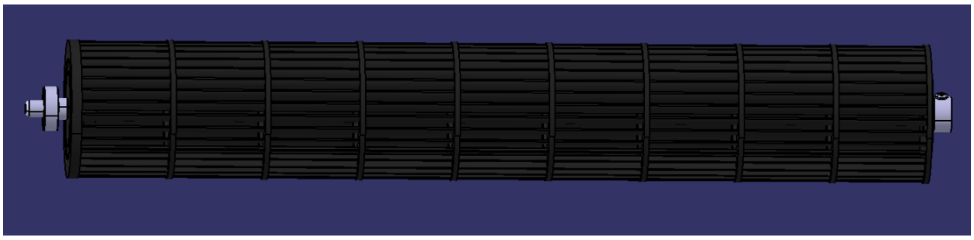

Figure 8.1: 500 mm turbine assembly considered in the rotor dynamic analysis.

The discretized model used for the calculations is illustrated schematically in Figure 8.2. For the actual 500 mm turbine analysis, the rotor was discretized into 10 disks (nodes A–J) connected by 9 beam elements (L1–L9). The beam element lengths correspond to the distances between consecutive nodes.

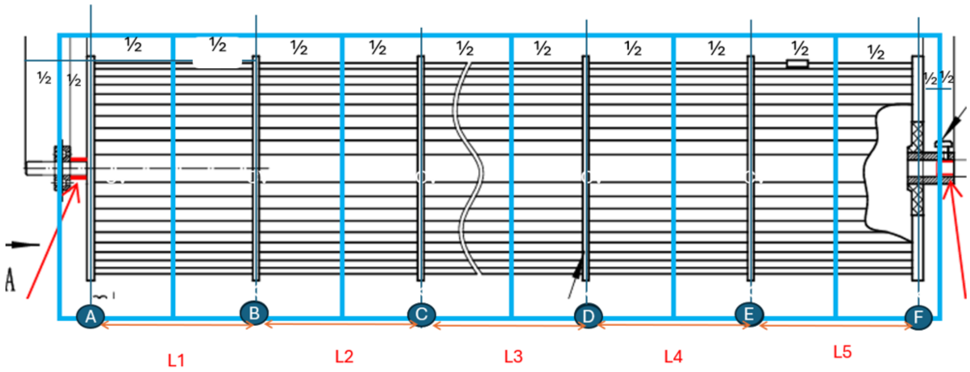

Figure 8.2: Simplified rotor discretization used for the analysis.

8.3 Model Assumptions

The following simplifying assumptions were adopted:

- Linear elastic material behaviour.
- Euler-Bernoulli beam theory.
- Lumped mass representation of the turbine wheel's disks.
- No damping effects included.
- No gyroscopic effects included.
- No aerodynamic loading included.
- Bearing flexibility neglected.

- The steel shaft sections located at both ends of the turbine were assumed to be infinitely rigid and therefore excluded from the flexible beam model.
- Only the plastic turbine body was considered to contribute to the bending flexibility of the rotor.

These assumptions were considered appropriate for a first-order engineering assessment intended to identify potential resonance risks within the operating range of the turbine.

Furthermore, the nodal masses included the mass contribution of the turbine wheel sections together with the associated shaft and spacer masses distributed between adjacent nodes. While the shaft and spacer masses were included in the mass matrix, their contribution to the bending stiffness was neglected. The flexible behaviour of the rotor was therefore assumed to be governed entirely by the plastic turbine body.

8.4 Determination of Model Parameters

The parameters required for the rotor dynamic model were obtained from the reconstructed CAD geometry of the turbine assembly. The geometric properties, mass distribution and beam dimensions were extracted directly from the CAD model and used as inputs for the finite-element formulation.

8.4.1 Determination of the Second Moment of Area

The bending stiffness of the turbine depends on the second moment of area of its cross-section.

A simplified estimate was first obtained by considering the blade cross-sections individually. The center of gravity of each blade section was measured with respect to the axis of rotation, as illustrated in Figure 8.3.

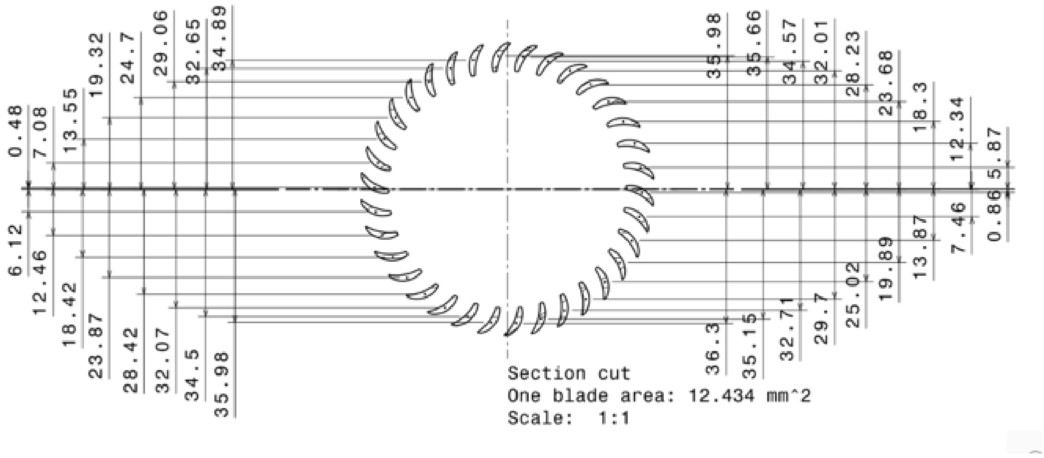

Figure 8.3: Blade centre-of-gravity locations used for estimation of the second moment of area.

The second moment of area was approximated using

$$I = \sum Ax^2$$

where A is the cross-sectional area of a blade and x is the distance between the blade centroid and the axis of rotation.

The resulting value was

$$I = 2.64 \times 10^{-7}\ m^4$$

8.4.2 Verification Using CATIA

The calculated value was compared with the inertia properties obtained directly from CATIA.

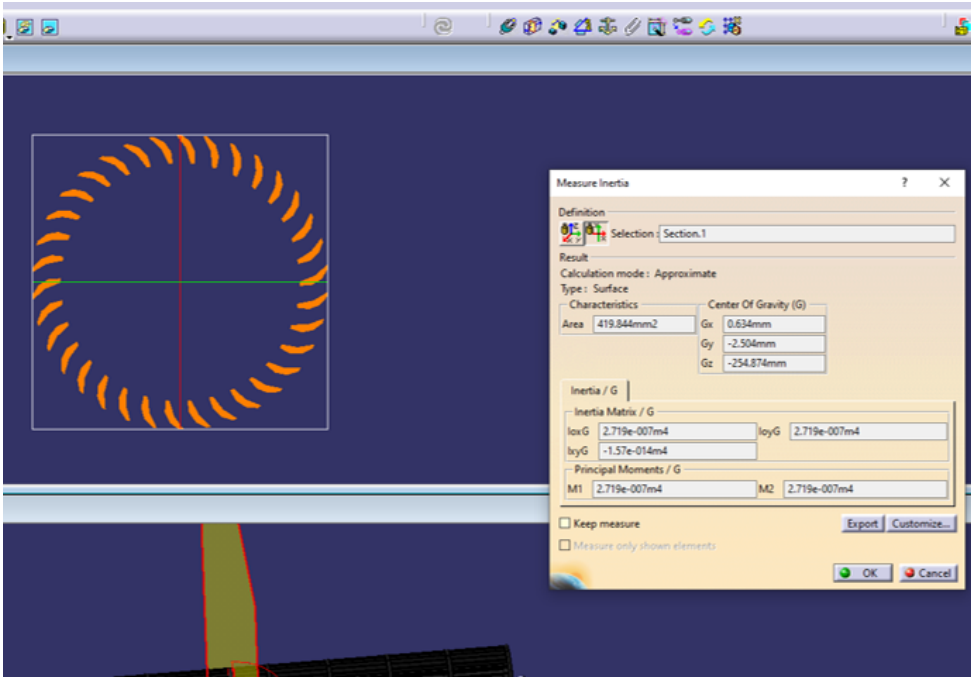

Figure 8.4: Moment of inertia obtained directly from CATIA.

CATIA provided

$$I = 2.719 \times 10^{-7}\ m^4$$

which showed good agreement with the manually calculated value.

Since the difference between both methods was small, the manually calculated value of

$$I = 2.64 \times 10^{-7}\ m^4$$

was adopted for the rotor dynamic analysis.

8.4.3 Material Properties

The turbine wheels are manufactured from AS30GFNH plastic.

The material properties used in the analysis were:

- Young's modulus:

$$E = 7.75 \times 10^9\ Pa$$

- Density:

$$\rho = 1200\ kg/m^3$$

These properties were used for the stiffness calculations and for the estimation of the turbine wheel masses. As previously indicated, for the mass matrix, the mass contributions of the bearings, steel shaft sections and steel spacers were also included and distributed to the corresponding nodes .

8.4.4 Beam Element Lengths

The distances between consecutive wheel sections were measured directly from the CAD model and used as beam element lengths.

The resulting element lengths for the 500 mm turbine are summarized in Table 8.1.

Table 8.1: Beam element lengths used in the rotor model.

Element	Length [mm]
L1	56.1
L2	54.8
L3	54.8
L4	54.8
L5	54.8
L6	54.8
L7	54.8
L8	54.8
L9	54.2

8.4.5 Mass Distribution

The mass matrix was constructed using a lumped-mass approach.

The nodal masses were obtained from the CAD model by assigning the corresponding wheel-section masses to each node.

The resulting nodal masses are summarized in Table 8.2.

Table 8.2: Nodal masses used in the rotor model.

Node	Mass [kg]
mA	0.078
mB	0.038
mC	0.038
mD	0.038
mE	0.038
mF	0.038
mG	0.038
mH	0.038
mI	0.038
mJ	0.054

In addition to the translational masses, a rotational inertia was assigned to each wheel section.

The blade centre-of-gravity radius was selected as the effective radius for the calculation of the rotational inertia because the majority of the wheel mass is distributed around this location.

The rotational inertia was therefore estimated using

$$J = mr^2$$

where m is the wheel-section mass and r is the distance between the blade centre of gravity and the axis of rotation.

Using the blade centre-of-gravity radius provides a reasonable first-order approximation of the actual mass distribution while maintaining a simple rotor model. The resulting rotational inertias were assembled into the rotary inertia terms of the global mass matrix.

8.5 Finite Element Formulation

The rotor was modelled using Euler-Bernoulli beam elements. Individual element stiffness matrices were assembled into a global stiffness matrix representing the complete turbine assembly.

The lumped masses were assembled into a corresponding global mass matrix.

The natural frequencies were obtained by solving the generalized eigenvalue problem:

$$[K]\{\phi\} = \omega^2[M]\{\phi\}$$

where:

- $[K]$ is the global stiffness matrix,
- $[M]$ is the global mass matrix,
- ω is the natural circular frequency,
- $\{\phi\}$ is the mode shape vector.

The calculations were implemented in Python.

8.6 Boundary Conditions

Each node of the beam model was assigned two degrees of freedom:

- Transverse displacement, w
- Rotation, θ

Since the 500 mm turbine was discretized into ten nodes, the resulting global system contained

$$2 \times 10 = 20$$

degrees of freedom.

The translational degrees of freedom at the two support locations were constrained in order to represent the turbine supports, while the rotational degrees of freedom remained free.

Consequently, two translational degrees of freedom were removed from the system, resulting in an 18×18 reduced stiffness matrix and mass matrix used for the eigenvalue solution.

The operating motor speed during normal operation was approximately 2000–2470 rpm, corresponding to an excitation frequency range of approximately 33–43 Hz.

The calculated natural frequencies were therefore compared directly with this operating frequency range.

8.7 Results

The first bending natural frequency obtained from the analysis is presented in Table 8.3.

Table 8.3: Rotor dynamic analysis results.

Parameter	Value
First natural frequency	336.6 Hz
Operating frequency range	33–43 Hz

8.8 Discussion

The first bending natural frequency of the turbine assembly was found to be approximately 336.6 Hz, which is significantly higher than the normal operating frequency range of the motor.

Based on the assumptions adopted in the simplified model, resonance associated with the first bending mode was therefore not expected during normal operation.

The analysis indicates that the operating frequency remains well separated from the first structural bending mode of the turbine. Consequently, the revised wheel assembly was not expected to introduce resonance-related issues associated with rotor bending.

It should be noted that the present analysis represents a first-order engineering estimate intended to evaluate the separation between operating and natural frequencies. More advanced models could include bearing flexibility, support compliance, damping effects, and gyroscopic behaviour in order to further refine the predictions.

Chapter 9

Prototype Development and Assembly

Following the CAD reconstruction, initial spacer adaptation strategy, axial positioning analysis, and procurement activities described in the previous chapters, a prototype of the revised turbine system was assembled. The objective of the prototype phase was to validate the mechanical integration of the redesigned system, verify assembly feasibility, and prepare the system for experimental testing. The "Short Chassis" configuration was chosen for the prototype unit.

9.1 Prototype Objectives

The prototype development phase was carried out with the following objectives:

- Validate the integration of the revised turbine system within the existing chassis architecture.
- Verify the compatibility of newly procured and reconstructed components.
- Confirm the functionality of the redesigned axial positioning system.
- Evaluate assembly repeatability and maintenance accessibility.
- Prepare a representative system for airflow and vibration measurements.

9.2 Prototype Preparation

The prototype assembly required a combination of existing chassis components, refurbished motors, newly procured components, and reconstructed elements identified during the CAD development phase.

Prior to assembly, the original motors were refurbished. The existing bearings were removed using appropriate extraction tools, motors were cleaned and installed with new bearings. The motors were subsequently reassembled, and prepared for integration with the turbine assemblies.

Several additional components required for the revised wheel assembly were procured, including springs, spacers, bearings, retaining elements, and fastening hardware.

Before assembly, all available components were inspected and compared against the reconstructed CAD models to verify dimensional compatibility and identify any potential integration issues.

9.3 Assembly Procedure

The assembly process began with preparation of the refurbished motor assemblies then continued with the preparation of the revised wheel assemblies.

The spacers, bearings, retaining elements, and spring components were subsequently assembled on the motor and the wheels (CW and CCW) according to the positions defined during the axial positioning study.

Following assembly of the rotating groups, and the installation of the motors to the casings, the revised assemblies were installed into the casings. Subsequently, the casings were closed, structural components such as stands, dampers were integrated on the casings and the completed turbine kits were then installed within the chassis structure.

Special attention was paid to the orientation of the turbine casings and the clockwise and counter clockwise turbine orientation to ensure the intended airflow direction through the side air channels of the rack cooling system. The electrical connections were configured accordingly to obtain the required rotation direction of the turbines.

9.4 Assembly Verification

Following assembly, several verification activities were performed.

The assembled turbines were manually rotated in order to verify freedom of movement and identify potential interference between rotating and stationary components.

The engagement of the redesigned spring system was verified throughout the assembly process. The assembly also confirmed the presence of the axial gap previously identified during the CAD analysis and demonstrated the necessity of the redesigned spring solution.

Visual inspection was performed to verify alignment between the turbine wheel, motor assembly, bearing locations, and casing interfaces.

These verification activities confirmed the overall feasibility of the proposed integration concept and allowed identification of potential issues requiring further investigation during experimental testing.

9.5 Assembly Documentation

An assembly document was prepared in parallel with the prototype development and testing activities.

The document includes the identification of the system components, required parts and tools, assembly sequences, reference CAD views, and instructions associated with the installation of the turbine assemblies.

The resulting documentation provides a repeatable assembly procedure and supports future maintenance, refurbishment, and large-scale deployment of the revised turbine system.

After the validation campaign, the assembly procedure was further refined and detailed. The resulting assembly document can be found in the appendices.

Chapter 10

Experimental Validation Methodology

The assembled prototype was experimentally evaluated in order to assess the performance of the revised turbine system, compare the results with the previous system and verify the assumptions made during the design phase.

The experimental campaign focused on two primary aspects:

- Airflow performance of the revised turbine configuration
- Mechanical vibration behaviour of the system

The measurements were performed using a fully assembled prototype operating under representative conditions. All prototype tests presented in this work were performed using a short-chassis configuration. The previous configuration used for comparison was also a short-chassis assembly in order to ensure consistency between the compared systems.

10.1 Test Objectives

The objectives of the experimental validation were:

- Verify that the revised turbine system provides sufficient airflow for the intended cooling application.
- Compare the airflow performance of the prototype against the previous configuration.
- Evaluate and validate the vibration behaviour of the revised system.
- Identify potential integration issues associated with the revised turbine assembly.
- Provide experimental feedback for further design improvements.

10.2 Experimental Setup

The prototype was operated using a standard 230 V AC supply and tested under steady-state operating conditions, initially on the floor, subsequently mounted on the rack.

Two measurement systems were used during the experimental campaign:

- A handheld anemometer for airflow measurements.
- A handheld vibrometer for vibration measurements.

10.3 Airflow Measurement Methodology

Airflow performance was evaluated using a handheld anemometer positioned at the outlet section of the turbine assembly.

Measurements were performed at multiple locations along the outlet opening in order to account for flow non-uniformities associated with the tangential fan configuration.

Velocity values were taken from both operating turbines. Both maximum and average air velocity values were recorded. The average velocity was subsequently used to estimate the volumetric flow rate of the assembly according to:

$$Q = v_{avg} \cdot A \tag{10.1}$$

where Q is the volumetric flow rate, v_{avg} is the measured average outlet velocity, and A is the outlet cross-sectional area obtained from the CAD model of the assembly.

The airflow performance of the revised prototype was compared with both the previous turbine configuration and the original fan performance curve provided by the manufacturer. The manufacturer curve relates volumetric flow rate (Q_v) to pressure increase (P_t) and is shown in Figure 10.1.

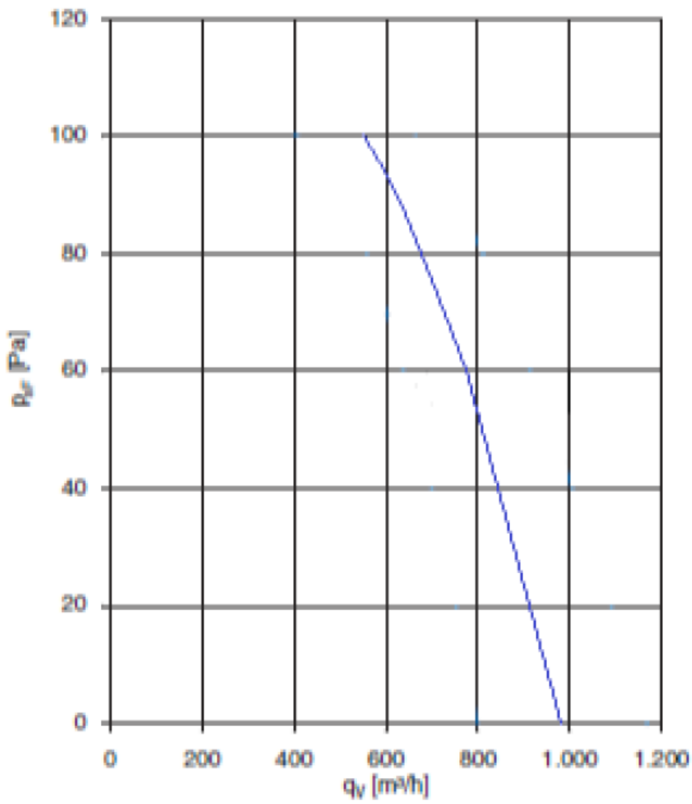

Figure 10.1: The manufacturer curve that relates volumetric flow rate to pressure increase

For comparison purposes, the operating condition corresponding to approximately zero pressure increase ($P_t \approx 0$ Pa) was considered. This assumption was made because the tests were performed in an open environment without the flow restrictions normally introduced by the rack electronics and internal airflow path.

Higher pressure values shown in the manufacturer curve represent operating conditions with increased flow resistance, such as those expected when the cooling air passes through electronic equipment and other rack components.

The pressure-loss characteristics of the original cooling system could not be accurately determined due to the limited availability of design documentation and the inability to obtain additional information from the original supplier. Therefore, the airflow comparison was performed using the free-flow operating condition ($P_t \approx 0$ Pa), which most closely represents the experimental setup used during this study.

The airflow measurements were primarily intended to verify that the redesigned turbine system maintained the air-moving capability of the original configuration and remained consistent with the expected performance range indicated by the manufacturer.

10.4 Vibration Measurement Methodology

The vibration behaviour of the system was evaluated using a handheld vibrometer with the following parameters:

- Measurement axis: 1 axis (along the sensor probe direction)
- Acceleration range (Peak): 0.1–199.9 m/s^2
- Velocity range (RMS): 0.1–199.9 mm/s
- Displacement range (Peak-to-Peak): 1–1999 μm
- Resolution:
  - Acceleration: 0.1 m/s^2
  - Velocity: 0.1 mm/s
  - Displacement: 1 μm
- Basic accuracy: $\pm$(5
- Dimensions: 185 $\times$ 68 $\times$ 30 mm
- Weight: 230 g

The vibration analysis was performed by comparing the revised prototype against the previous turbine configuration. Between the two configurations, only the turbine and motor related components (revised components) were modified, while the remaining structural components, including the chassis, dampers and casing, were kept unchanged. This approach allowed the influence of the revised assembly to be assessed while minimizing the effect of external variables.

The tested prototype configuration included:

- Refurbished motors (the two internal bearings were replaced and the motors were subsequently reassembled)
- New springs
- New spacers
- New plastic turbine wheels

The previous configuration included:

- Unused (non-refurbished) motors

- Original springs
- Original turbine wheel assemblies (without spacers)

All components of the previous configuration were unused.

In order to improve measurement repeatability, the sensor was attached to the same screw locations on either the chassis or the casing throughout the test campaign. These locations were selected because most of the structure was manufactured from non-magnetic materials, whereas the selected mounting points allowed repeatable sensor positioning through magnetic attachment. For measurements performed on the top surface of the casing, since the casing's top surface is non magnetic, the probe was manually positioned at the same location during each test.

The chassis was positioned directly on the floor during the initial measurements and operated under steady-state conditions. Subsequently, the assembly was installed in the rack and the remaining measurements were performed under the same operating conditions.

For each configuration, at least three measurements were performed in order to evaluate measurement repeatability and account for fluctuations during operation.

The measured vibration levels were compared using reference vibration severity ranges derived from ISO 20816 / ISO 10816 (Mechanical vibration - Measurement and evaluation of machine vibration)[8, 7]. Since the tested assembly does not fully correspond to the machine classifications defined by the standard, the ISO 20816 / ISO 10816 limits were used for reference purposes only and not as a formal acceptance criterion.

Two configurations were initially investigated:

- Previous turbine configuration
- Revised prototype configuration

As the experimental campaign progressed, additional investigations were performed, including motor and case swap tests, wheel removal tests, assembly preload studies and support-condition evaluations. These additional tests were conducted to identify the origin of the measured vibration and separate the influence of the wheel assembly, motor assemblies and structural support conditions.

The vibration measurements were therefore used as a comparative indicator of the dynamic behaviour of the assemblies and to identify potential sources of imbalance, misalignment, assembly preload effects and support-condition sensitivities requiring further investigation.

10.4.1 Identification of Measurement Locations

To ensure consistency throughout the vibration investigation, measurements were performed at predefined locations on the chassis and turbine cases. The same locations were used whenever possible during all tests, allowing direct comparison between different assembly configurations.

Figure 10.2 illustrates the measurement locations used during the experimental campaign.

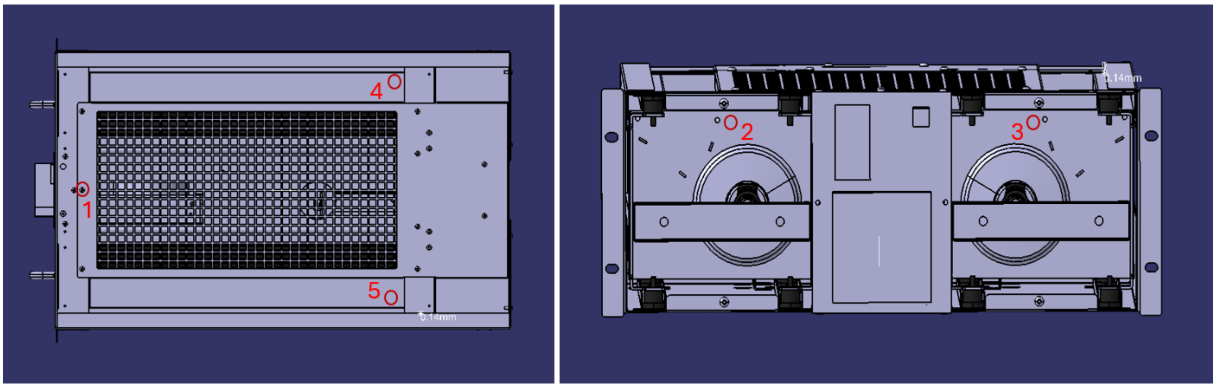

Figure 10.2: Identification of vibration measurement locations used during the experimental validation campaign.

The selected measurement locations were:

1. Chassis Top

2. Left Case Front

3. Right Case Front

4. Left Case Top

5. Right Case Top

The Chassis Top location was used as the primary reference location throughout the investigation, because it exhibited the largest response to assembly modifications and therefore provided the clearest indication of the overall vibration behaviour of the complete system.

The Case Top and Case Front locations were used to identify the contribution of individual turbine assemblies and to distinguish local vibration sources from vibration transmitted through the chassis structure.

Chapter 11

Results and Discussion

11.1 Airflow Performance

The airflow performance of the revised turbine assembly was evaluated experimentally and compared with both the previous configuration and the available manufacturer performance data of the original turbine system.

Air velocity measurements were performed at multiple locations along the turbine outlet and representative average values were recorded. The measured outlet velocities were converted into volumetric flow rates using the outlet cross-sectional area obtained from the CAD models.

Figure 11.1 presents the comparison between the measured airflow performance and the manufacturer performance curve available for the original turbine system.

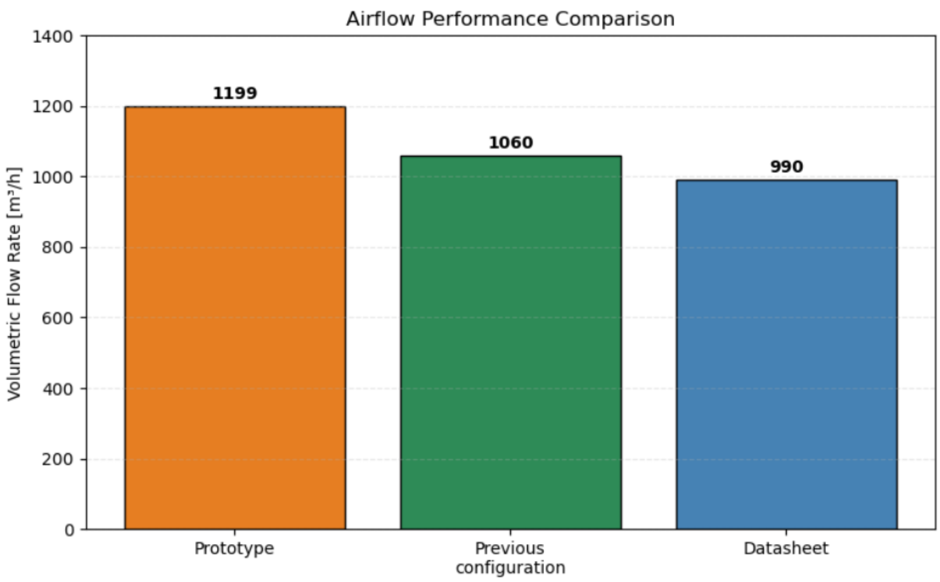

Figure 11.1: Comparison of measured airflow performance with manufacturer data.

Since the tests were performed without representative electronic equipment installed in the rack, the operating pressure was assumed to be approximately zero as explained in Section 10.3. The average outlet air velocity was measured as approximately 13 m/s for the revised prototype and 11.5 m/s for the previous configuration. Using the outlet area obtained from the CAD model, $A = 0.02562, \mathrm{m}^2$, the corresponding volumetric flow rates were calculated as approximately 1199 m^3/h for the prototype and 1060 m^3/h for the previous configuration.

The datasheet value of the original system at approximately zero pressure increase is about 990 m^3/h. Therefore, both measured configurations were within the expected airflow range, and the revised prototype showed a slightly higher estimated volumetric flow rate than the previous configuration.

The results demonstrated that the revised turbine assembly maintained airflow performance comparable to the original system and therefore satisfied the primary design objective of preserving cooling capability while enabling integration of the revised wheel assembly.

11.2 Motor Electrical Behaviour

To verify that the prototype motors were operating under conditions comparable to those of the previous configuration, current and supply voltage measurements were analysed during operation.

Figures 11.2 and 11.3 show representative measurements obtained from an unused motor from the previous configuration and from the prototype assembly.

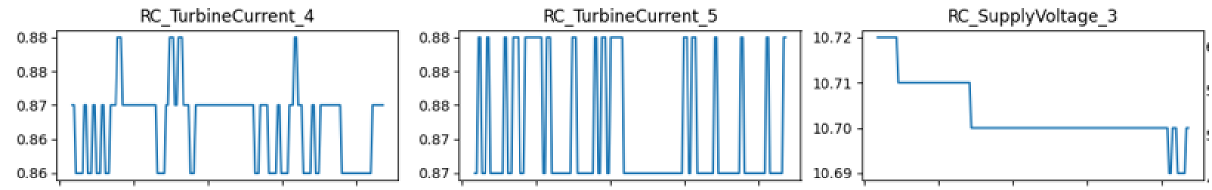

Figure 11.2: Representative current (A) and supply voltage (V) measurements of an unused previous-configuration motor pair, Test duration: 10 minutes, X axis: Time.

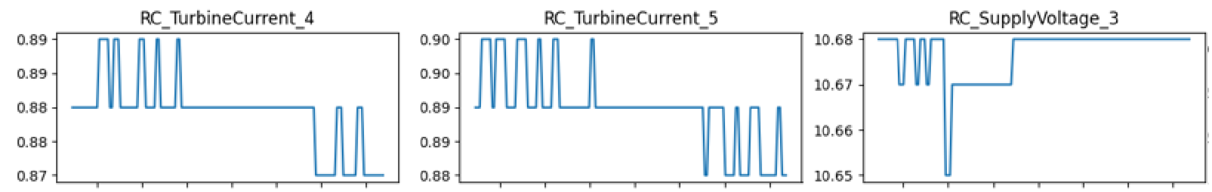

Figure 11.3: Representative current (A) and supply voltage (V) measurements of the prototype's refurbished motor pair, Test duration: 10 minutes, X axis: Time.

The measured current and voltage values remained stable throughout operation and were consistent with those measured for the unused motors of the previous configuration. Consequently, the elevated vibration levels observed in the prototype could not be attributed to differences in motor electrical supply conditions.

11.3 Initial Vibration Assessment

The first vibration measurements revealed a significant difference between the prototype and the previous configuration.

Figure 11.4 presents the initial comparison between the two systems.

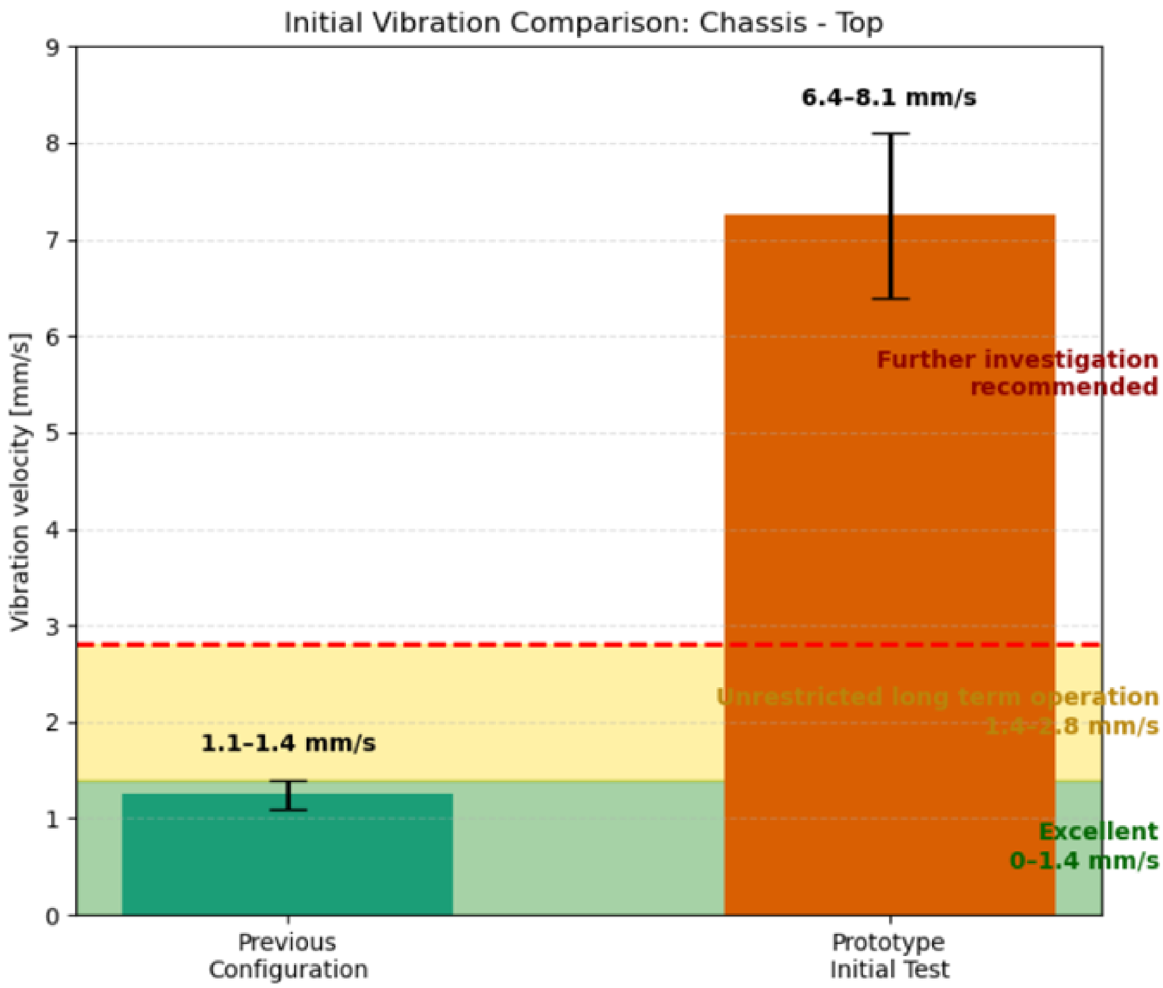

Figure 11.4: Initial vibration comparison between prototype and previous configuration.

The previous configuration produced stable vibration levels between approximately 1.1 and 1.4 mm/s at the chassis-top location. In contrast, the prototype exhibited vibration levels between approximately 6.4 and 8.1 mm/s, corresponding to roughly five to seven times higher vibration.

These results initiated a systematic investigation to identify the source of the elevated vibration response.

11.4 Investigation of Potential Vibration Sources

Several possible sources of vibration were investigated sequentially.

11.4.1 Bearing Relative Motion

Visual inspection revealed relative motion between the turbine shaft and the bearing inner ring. To investigate its influence, the bearing inner rings were bonded to the shaft using Loctite 638 retaining compound.

Figure 11.5 presents the measured vibration levels before and after bonding.

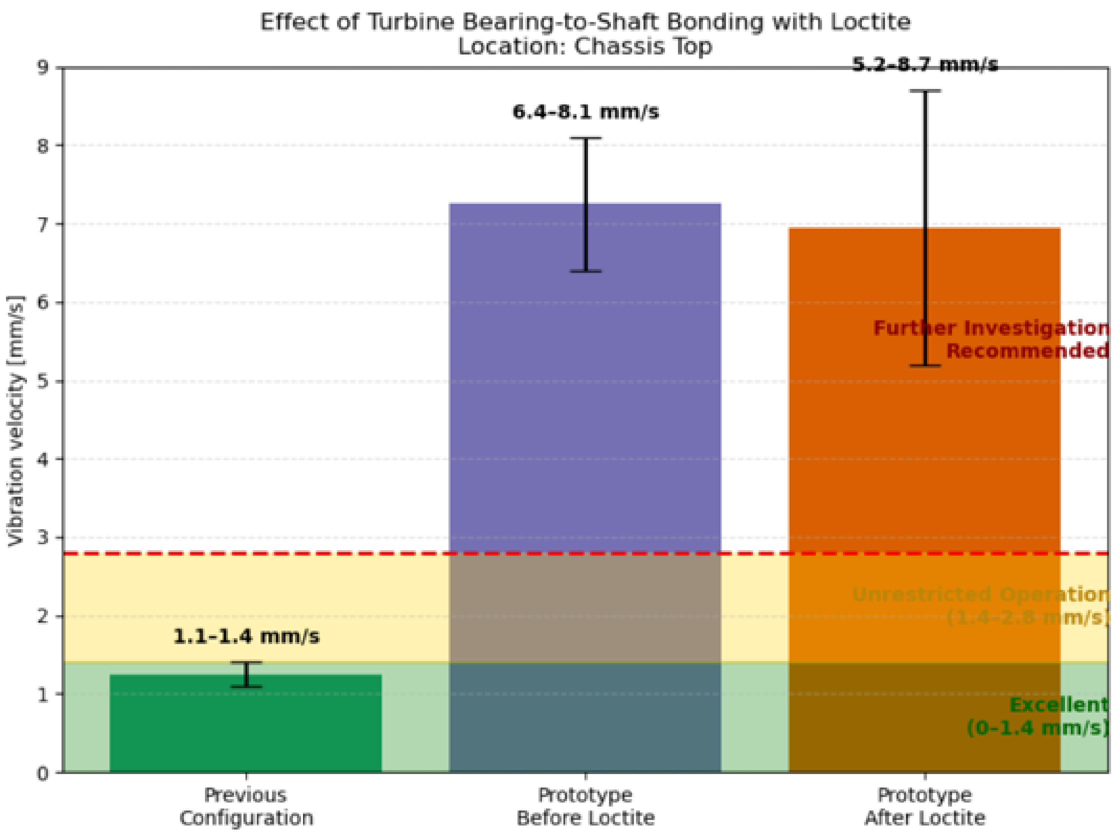

Figure 11.5: Influence of bearing-shaft bonding on vibration response.

Only a small reduction in vibration was observed. High vibration levels and large fluctuations remained, indicating that the primary excitation source originated elsewhere.

11.4.2 Vibration Measurements at all Pre-Selected Measurement Locations

Following the limited reduction obtained after bonding the bearing inner rings to the shaft using Loctite 638, vibration measurements were repeated at all predefined measurement locations. The aim of this test was to compare the vibration response of the revised prototype with the previous configuration and identify the most critical measurement locations for the following investigation.

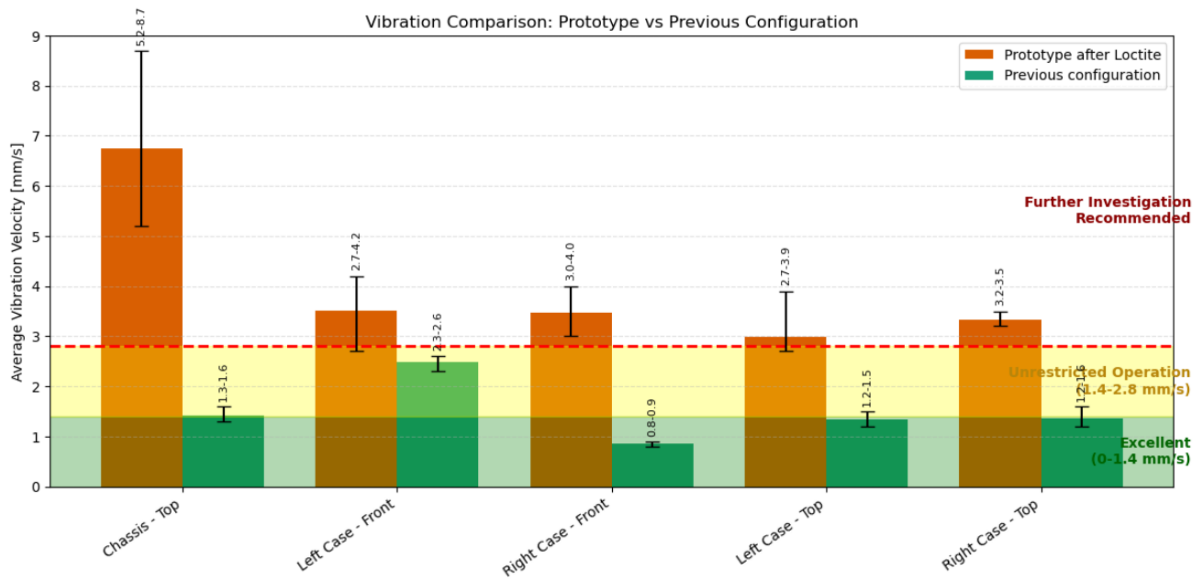

Figure 11.6: Comparison of vibration levels between the prototype assembly after Loctite application and the previous configuration at all predefined measurement locations.

As shown in Figure 11.6, the prototype exhibited significantly higher vibration levels than the previous configuration at all measured locations. The highest vibration response was measured at the Chassis-Top location, where the prototype reached approximately 5.2–8.7 mm/s, while the previous configuration remained within approximately 1.3–1.6 mm/s.

The Chassis-Top measurement point also showed the largest fluctuation range. This indicated that the chassis response was highly sensitive to the excitation generated by the prototype assembly and therefore represented the most critical location for the following vibration investigation.

At the case-front and case-top locations, the prototype also showed higher vibration levels than the previous configuration. However, the difference was less pronounced than at the chassis-top location. This suggested that the elevated response was not only a local vibration issue, but involved the dynamic interaction between the turbine assemblies and the supporting chassis structure.

Based on these results, the Chassis-Top location was selected as the primary reference point for the following root-cause investigation and validation tests.

11.4.3 Influence of Individual Turbine Assemblies

Additional tests were performed to the prototype by operating the left and right turbine assemblies separately. The objective was to determine whether one turbine assembly contributed disproportionately to the elevated vibration response observed in the prototype.

During these tests, the opposite turbine assembly was removed and vibration measurements were recorded only at locations associated with the operating turbine. For example, left-side measurements were recorded during left-turbine operation and right-side measurements during right-turbine operation.

Figure 11.7 presents the measured vibration levels for the isolated turbine assemblies.

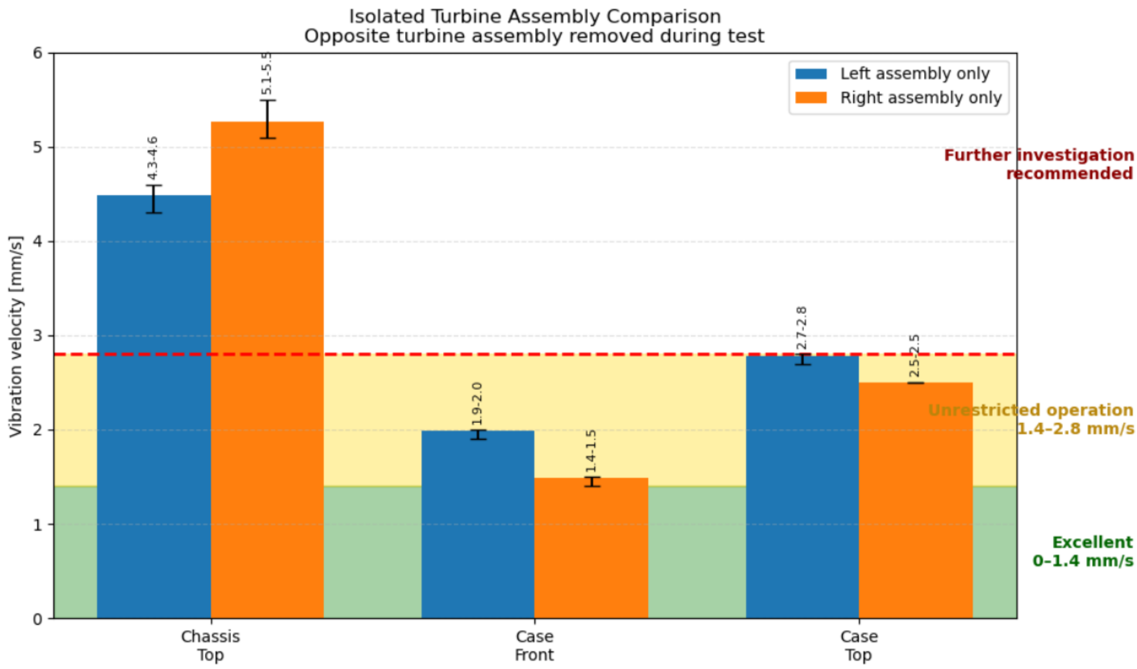

Figure 11.7: Vibration measurements obtained during isolated operation of the left and right turbine assemblies.

The results showed that both turbine assemblies produced elevated vibration levels at the Chassis-Top measurement location. The left assembly generated vibration levels between approximately 4.3 and 4.6 mm/s, while the right assembly produced slightly higher values between approximately 5.1 and 5.5 mm/s.

At the Case-Front measurement location, vibration levels remained relatively low and close to the reference vibration limits, ranging between approximately 1.4 and 2.0 mm/s. Similarly, the Case-Top measurements remained significantly lower than the corresponding Chassis–Top values, with measured vibration levels between approximately 2.5 and 2.8 mm/s.

An additional observation was that measurement fluctuations decreased significantly compared to the previous tests where both turbines were operating simultaneously. This indicated that, the interaction between the two assemblies contributed to the fluctuations observed during the initial measurements.

The relatively small difference between the left and right turbine assemblies suggests that neither turbine alone was solely responsible for the elevated vibration response.

Additionally, the consistently higher vibration levels measured at the Chassis-Top location indicate that the chassis structure may be locally amplifying the vibration transmitted by the turbine assemblies.

Based on these results, both turbine assemblies were retained as potential contributors to the overall vibration response, and further investigations were performed to isolate the influence of the wheel assemblies, motors and supporting structure.

11.4.4 Investigation of the Motor/Case Assembly Without Turbine Wheels

To determine whether the elevated vibration levels originated from the turbine wheels or from the motor/case assembly itself, the turbine wheels of the prototype were completely removed and the system was operated using only the motor and casing assemblies.

Initially, the measurements were performed with the assembly placed directly on the floor. The vibration response was measured at the Chassis-Top location, which had previously exhibited the highest vibration levels.

Figure 11.8 presents the results obtained during the floor-mounted tests.

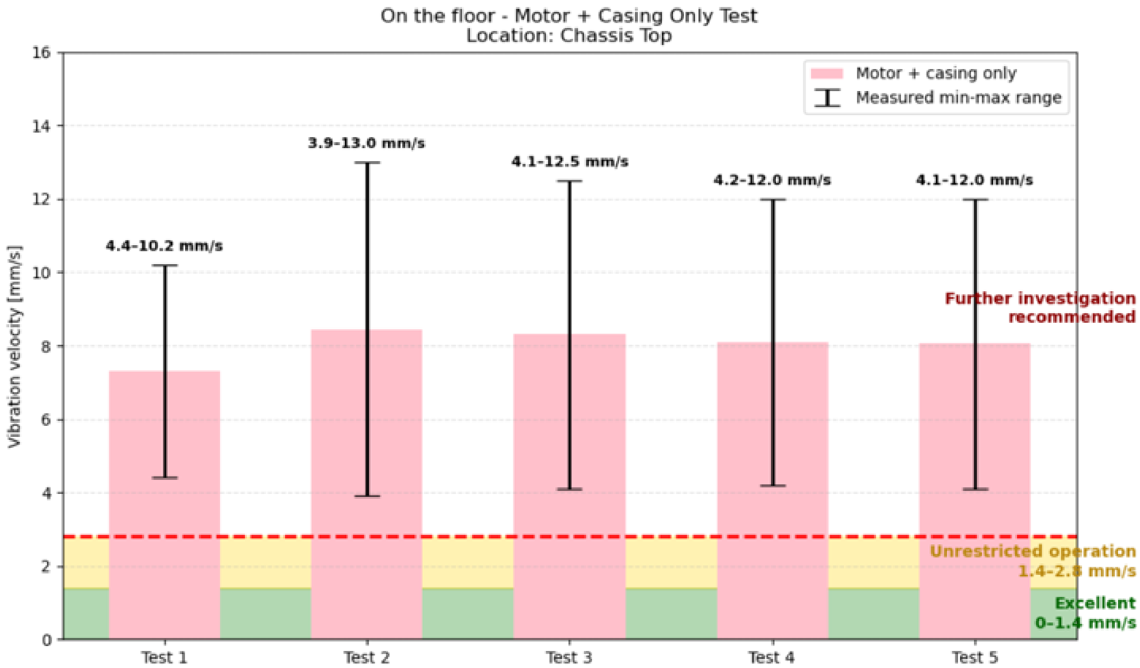

Figure 11.8: Motor and casing assembly tested without turbine wheels on the floor.

Despite the complete removal of the turbine wheels, significant cyclic vibration behaviour remained present. The measured vibration fluctuated between approximately 3.9 and 13.0 mm/s, indicating that the main excitation source wasn't exclusively associated with the revised wheel assembly.

Since the final operating condition of the cooling system corresponds to rack installation, all subsequent vibration investigations were performed with the chassis mounted inside the rack.

The wheel-less motor/case assembly test was therefore repeated after installation of the chassis in the rack.

Figure 11.9 presents the corresponding results.

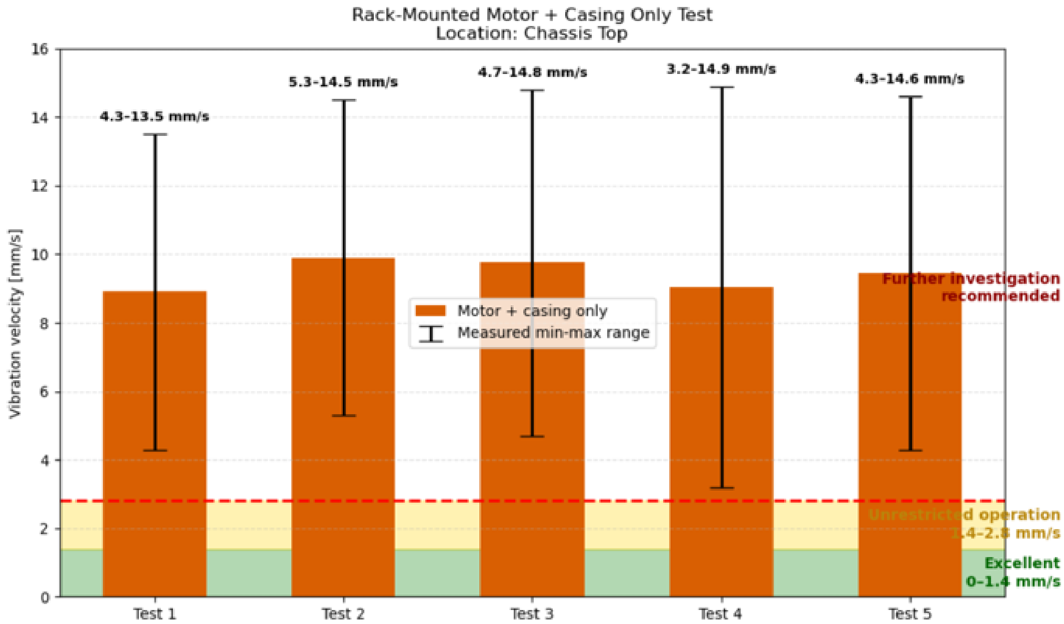

Figure 11.9: Motor and casing assembly tested without turbine wheels after installation in the rack.

The cyclic behaviour remained present after rack installation. Vibration levels fluctuated between approximately 3.2 and 14.9 mm/s. During these tests, manually applying force to the chassis reduced the audible noise but did not eliminate the vibration cycles. This observation suggested that the chassis contributed to the amplification of the vibration response, while the primary excitation source remained within the motor/case assembly.

To further isolate the source of the vibration, the left and right motor/case assemblies were subsequently operated individually while still installed in the rack.

Figure 11.10 shows the results obtained during these measurements.

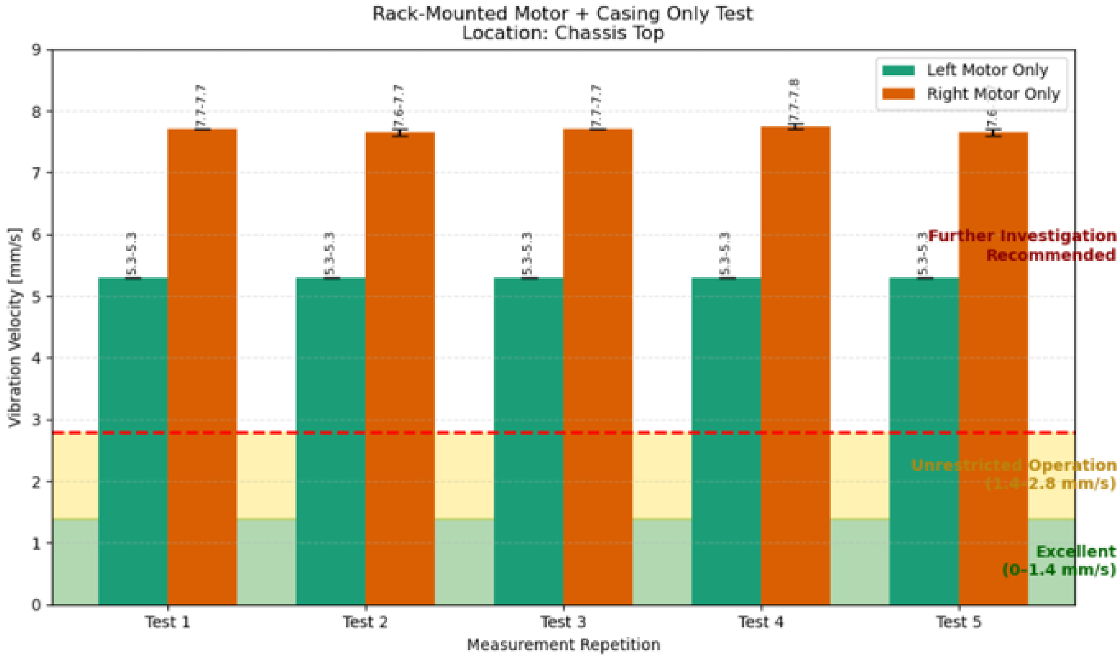

Figure 11.10: Individual motor/case assembly measurements without turbine wheels.

The individual measurements revealed highly stable vibration levels with significantly reduced fluctuations compared to the previous tests. However, the vibration magnitude remained high. The left motor/case assembly produced vibration levels of approximately 5.3 mm/s, while the right motor/case assembly consistently produced values between approximately 7.6 and 7.8 mm/s at the Chassis-Top location.

The reduction of the cyclic fluctuations during individual operation suggests that the previously observed oscillations may have been influenced by the simultaneous operation of two vibration sources with similar excitation frequencies. Such behaviour is commonly associated with beat phenomena, where two closely spaced similar but not the same frequencies periodically reinforce and cancel each other, producing cyclic amplitude variations [10].

Nevertheless, the high vibration levels observed during individual operation demonstrate that the beat phenomenon itself cannot be considered the root cause of the elevated vibration response. Instead, it only explains the cyclic fluctuation observed during simultaneous operation. The primary source of vibration was already present when each motor/case assembly was operated independently.

Since all tests described in this section were performed without turbine wheels, the results strongly suggest that the wheel assemblies, springs, spacers and wheel-to-motor interfaces were not the primary contributors to the elevated vibration levels observed in the prototype.

Based on these findings, the subsequent investigation focused on the interaction between the motor assemblies, casing structure and chassis support conditions.

11.4.5 Investigation of Circlip Seating

Visual inspection suggested that one motor circlip might not be fully seated within its groove. The circlip was pressed into position and the measurements were repeated.

No significant change in vibration levels was observed. The circlip seating was therefore excluded as a significant contributor to the measured vibration.

11.4.6 Investigation of the Prototype Chassis

To determine whether the prototype chassis itself was responsible for the elevated vibration response, the complete previous-configuration motor/case/wheel assemblies were installed into the prototype chassis.

The resulting chassis-top vibration remained low and stable between approximately 0.9 and 1.3 mm/s.

This result demonstrated that the prototype chassis alone was not responsible for the elevated vibration levels.

11.4.7 Influence of Wheel Removal and Assembly Preload

Following the confirmation that the prototype chassis itself was not responsible for the elevated vibration levels, additional investigations were performed to determine whether the vibration originated from the turbine wheels or from the motor/case assemblies.

Since the prototype motor/case assemblies had already been tested without turbine wheels, a comparable test was required for the previous configuration. Therefore, the turbine wheels were also removed from the previous-configuration assemblies and the vibration measurements were repeated. All measurements presented in this section correspond to the Chassis-Top measurement location, which had previously shown the highest vibration levels.

Before wheel removal, baseline measurements were recorded for the previous left and previous right assemblies operating individually with their original wheel assemblies installed. These measurements are shown in Figure 11.11.

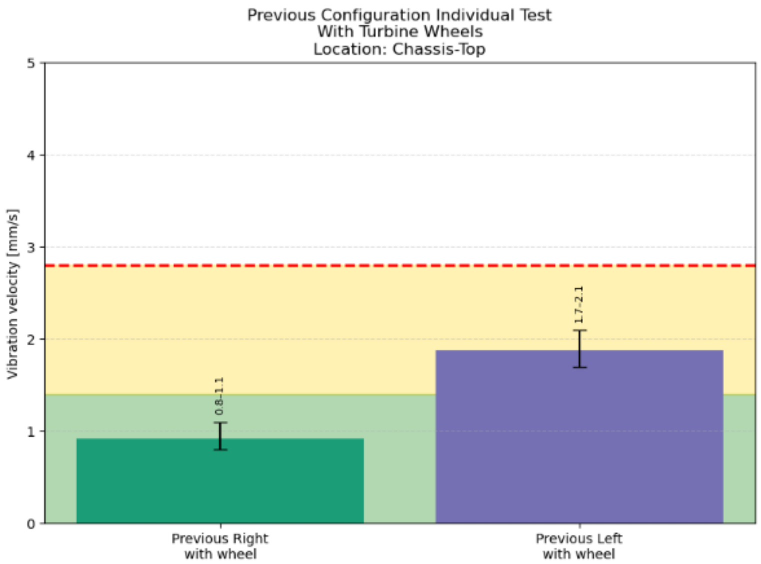

Figure 11.11: Previous-configuration assemblies operating individually with turbine wheels installed.

After wheel removal and reassembly, the behaviour of the two previous-configuration assemblies differed significantly.

The previous left assembly became significantly more sensitive after wheel removal. During reassembly it was observed that the case holes no longer aligned naturally and additional force was required to install the final screw.

The initial reassembly without torque control increased the vibration level from approximately 1.7–2.1 mm/s to 3.2–3.3 mm/s. An attempt to adjust the support stands increased the vibration further to approximately 3.7–4.3 mm/s. When the assembly was subsequently reassembled using a controlled case screw torque of 1.5 Nm, the vibration level decreased to approximately 2.3–2.7 mm/s (Figure 11.12).

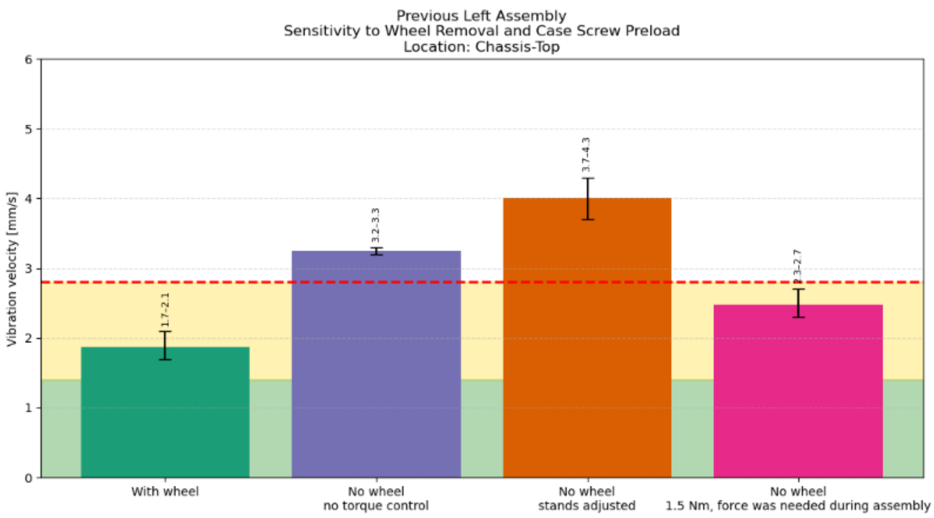

Figure 11.12: Influence of reassembly conditions on the previous left assembly after wheel removal.

These observations suggested that the vibration response was strongly affected by assembly preload and case screw tightening conditions.

Subsequently, tightening torque control was applied to the previous right assembly and its vibration levels remained largely unchanged. The vibration level decreased slightly from approximately 0.8–1.1 mm/s to 0.6–0.7 mm/s, indicating that wheel removal had little influence on its vibration response (Figure 11.13).

Figure 11.13: Previous right assembly before and after wheel removal.

To determine whether a similar effect existed in the prototype assembly, the same controlled tightening procedure was applied to the prototype right motor/case assembly without wheels. Before torque control, vibration levels fluctuated between approximately 7.2 and 7.7 mm/s. After reassembly using controlled tightening (1.5 Nm case screws), the vibration level decreased to approximately 3.4–3.8 mm/s, corresponding to roughly a 50% reduction (Figure 11.14).

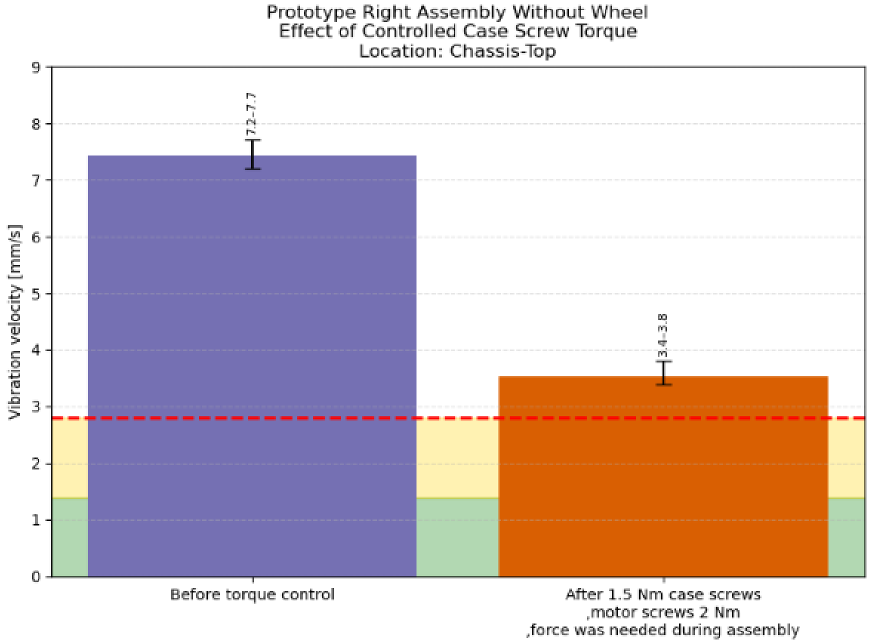

Figure 11.14: Effect of controlled tightening on the prototype right motor/case assembly.

Figure 11.15 summarizes the most relevant results obtained during the investigation.

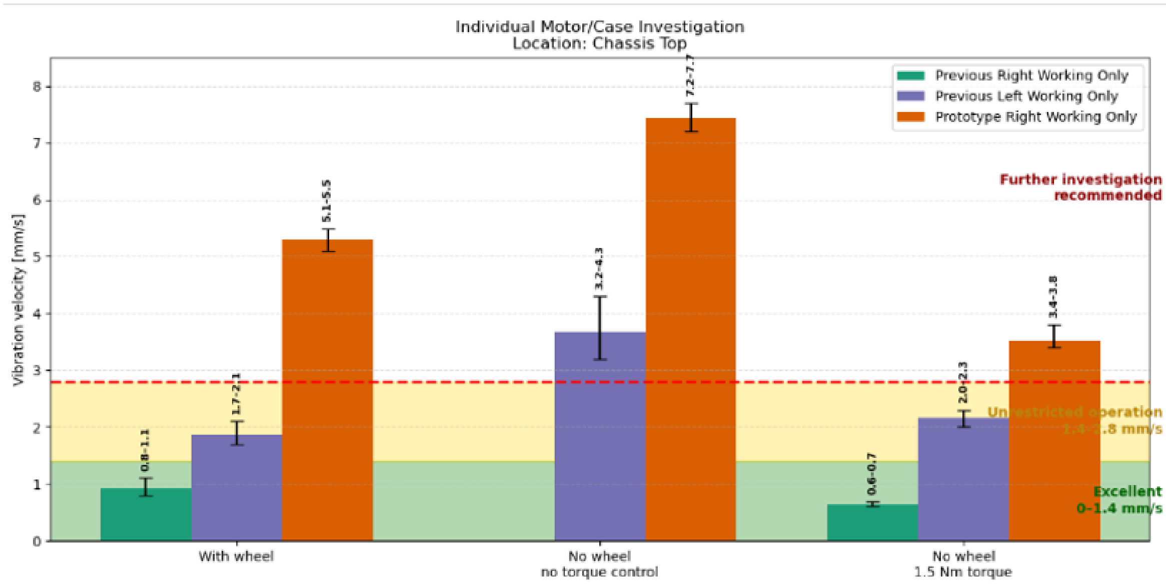

Figure 11.15: Summary of wheel-removal and torque-control investigations.

The results demonstrate that assembly conditions can significantly influence the measured vibration levels. Controlled tightening consistently reduced vibration in both the previous and prototype assemblies, indicating that case preload and structural alignment contribute substantially to the dynamic behaviour of the system.

Consequently, the investigation was continued with a focus on the interaction between the motor assemblies, casing structure, and support conditions.

11.4.8 Motor and Case Swap Tests

Motor/case swap tests were performed to separate the influence of the refurbished motors from that of the supporting case. Tests were conducted on the right motor/case assemblies of both the prototype and the previous configuration.

Figure 11.16 presents the results.

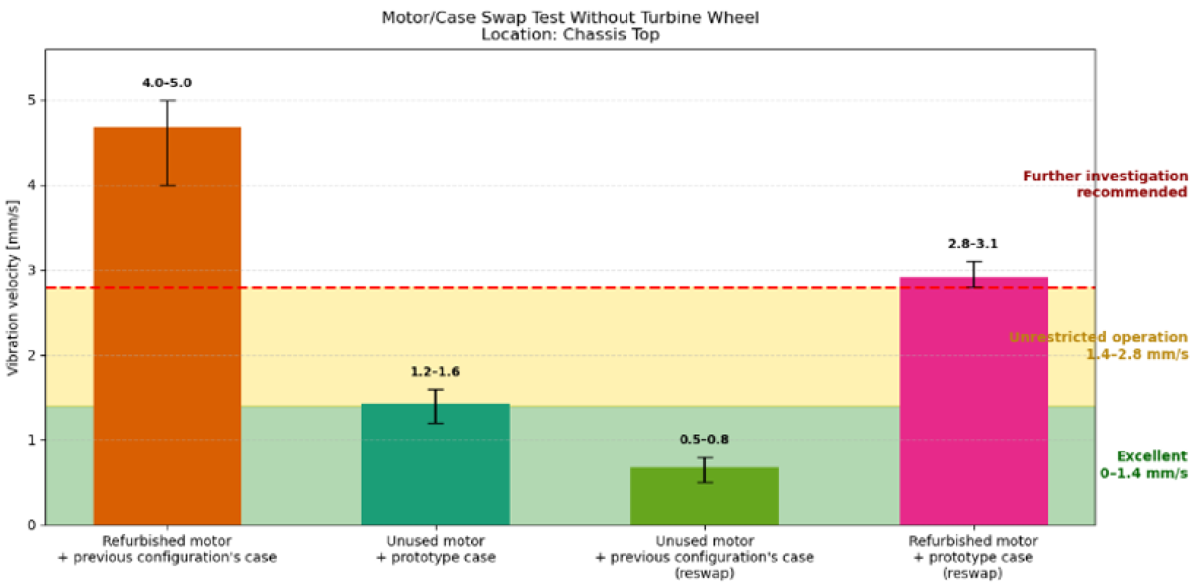

Figure 11.16: Motor and case swap test results.

The vibration increase consistently followed the refurbished motors regardless of which case was used. This demonstrated that the dominant excitation source was associated with the refurbished motor assemblies rather than the prototype case.

However, the measured vibration amplitude still depended on the case and assembly condition, and contrary to expectations, the healthy previous configuration case did not produce lower vibration levels with the refurbished motor. When the refurbished motor was installed, the healthy case exhibited higher vibration than the prototype case. This suggests that the vibration response is influenced by the combined motor-case system rather than by the condition of the case alone. The motor, structural stiffness distribution, assembly preload, and support conditions likely interact to determine the final vibration level.

11.5 Prototype Wheel Validation

Following the previous investigations, it was concluded that the elevated vibration levels observed in the prototype were primarily associated with the refurbished motor/case assemblies and assembly conditions rather than the revised wheel design itself.

To isolate the influence of the wheel assembly, the prototype wheels were installed on healthy, unused motor/case assemblies from the previous configuration. The assembly procedures developed during the preload investigation were applied throughout the validation process.

Figure 11.17 presents the results obtained during the prototype wheel validation tests.

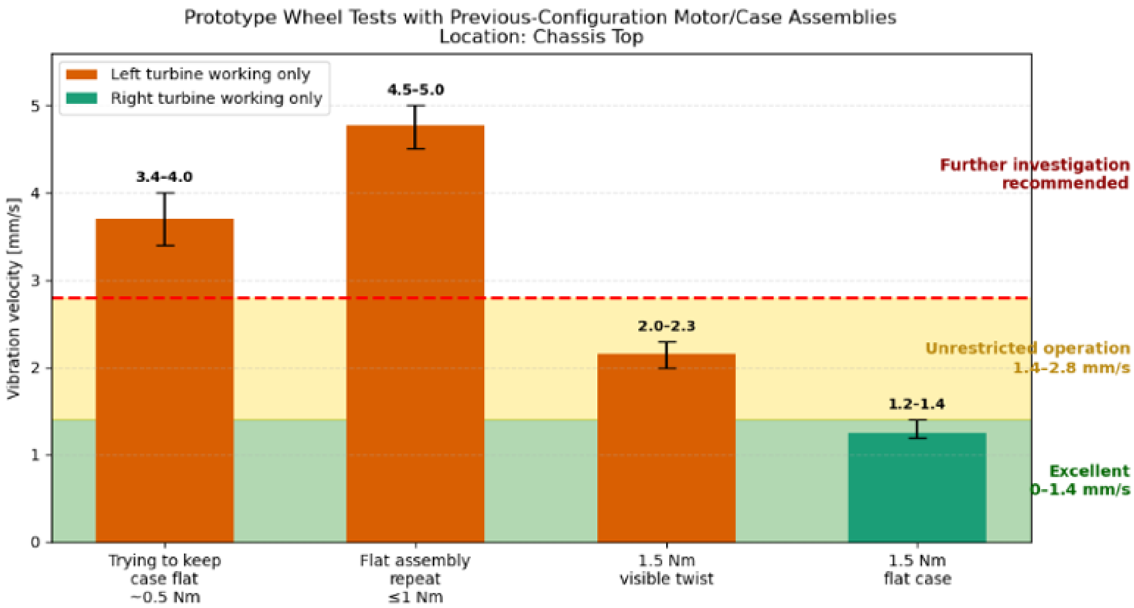

Figure 11.17: Validation of the prototype wheel assembly using healthy previous-configuration motor/case assemblies.

The right-side assembly, whose casing naturally aligned during assembly, produced stable vibration levels of approximately 1.2–1.4 mm/s when assembled using a controlled tightening torque of 1.5 Nm.

The left-side assembly remained significantly more sensitive to assembly conditions. Attempts to maintain a visually flat casing by adjusting tightening torque produced vibration levels between approximately 3.4 and 5.0 mm/s. Although controlled tightening reduced the vibration to approximately 2.0–2.3 mm/s, the results remained significantly higher than those obtained from the right-side assembly.

During these tests it was repeatedly observed that the screw holes of the left-side casing did not align naturally after reassembly. Equal tightening torque therefore introduced visible casing twist and assembly preload. These observations further confirmed that local assembly conditions and structural distortion had a major influence on the measured vibration response.

Consequently, an additional investigation was performed to determine whether a local support condition was responsible for the remaining vibration increase.

11.5.1 Investigation of Local Support Conditions

Inspection of the left-side assembly revealed a visible support gap between the chassis and one of the casing's vibration dampers. It was hypothesized that this gap allowed decreased the stiffness of the structure and contributed to the elevated vibration levels.

To evaluate this hypothesis, a temporary spacer manufactured from hard paper was inserted at the gap location.

Figure 11.18 summarizes the results.

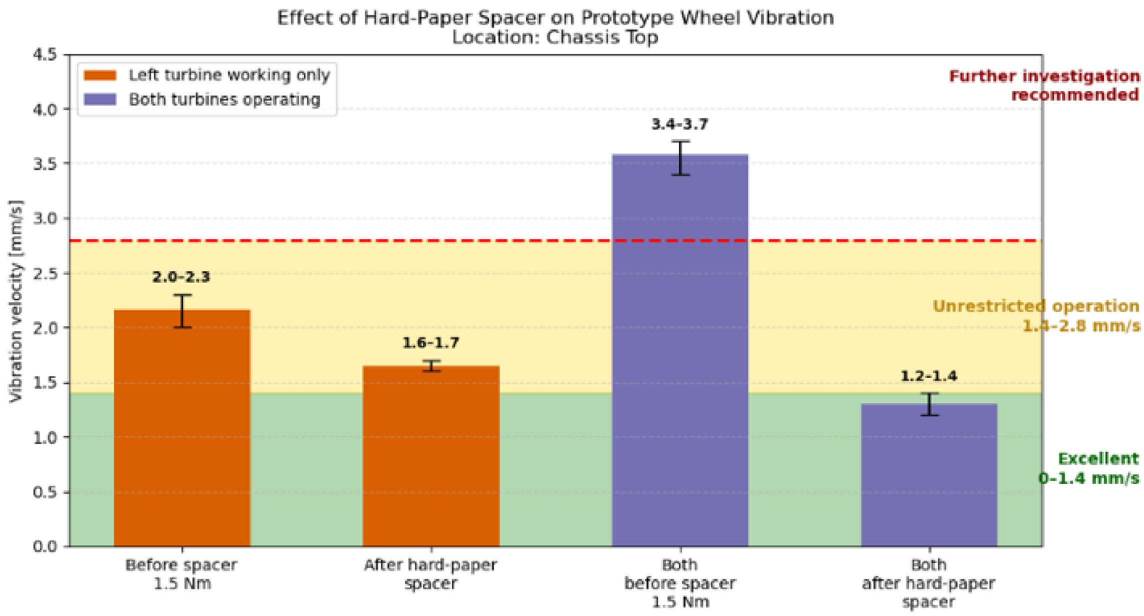

Figure 11.18: Effect of the temporary spacer on measured vibration levels.

For the left turbine operating individually, the vibration level decreased from approximately 2.0–2.3 mm/s to 1.6–1.7 mm/s after installation of the spacer.

When both turbines were operated simultaneously, the vibration level decreased from approximately 3.4–3.7 mm/s to 1.2–1.4 mm/s.

These results demonstrated that the local support condition had a significant influence on the vibration response of the assembly. Eliminating the support gap reduced the measured vibration to values comparable to those of the previous configuration, indicating that the remaining vibration increase was primarily associated with assembly-induced deformation rather than the wheel design itself.

The temporary spacer used during the validation tests consisted of a hard-paper washer with an outer diameter of 16 mm and a thickness of approximately 1.6 mm. The spacer was positioned between the casing support and the damper at the location where the gap was observed, see Figure 11.19.

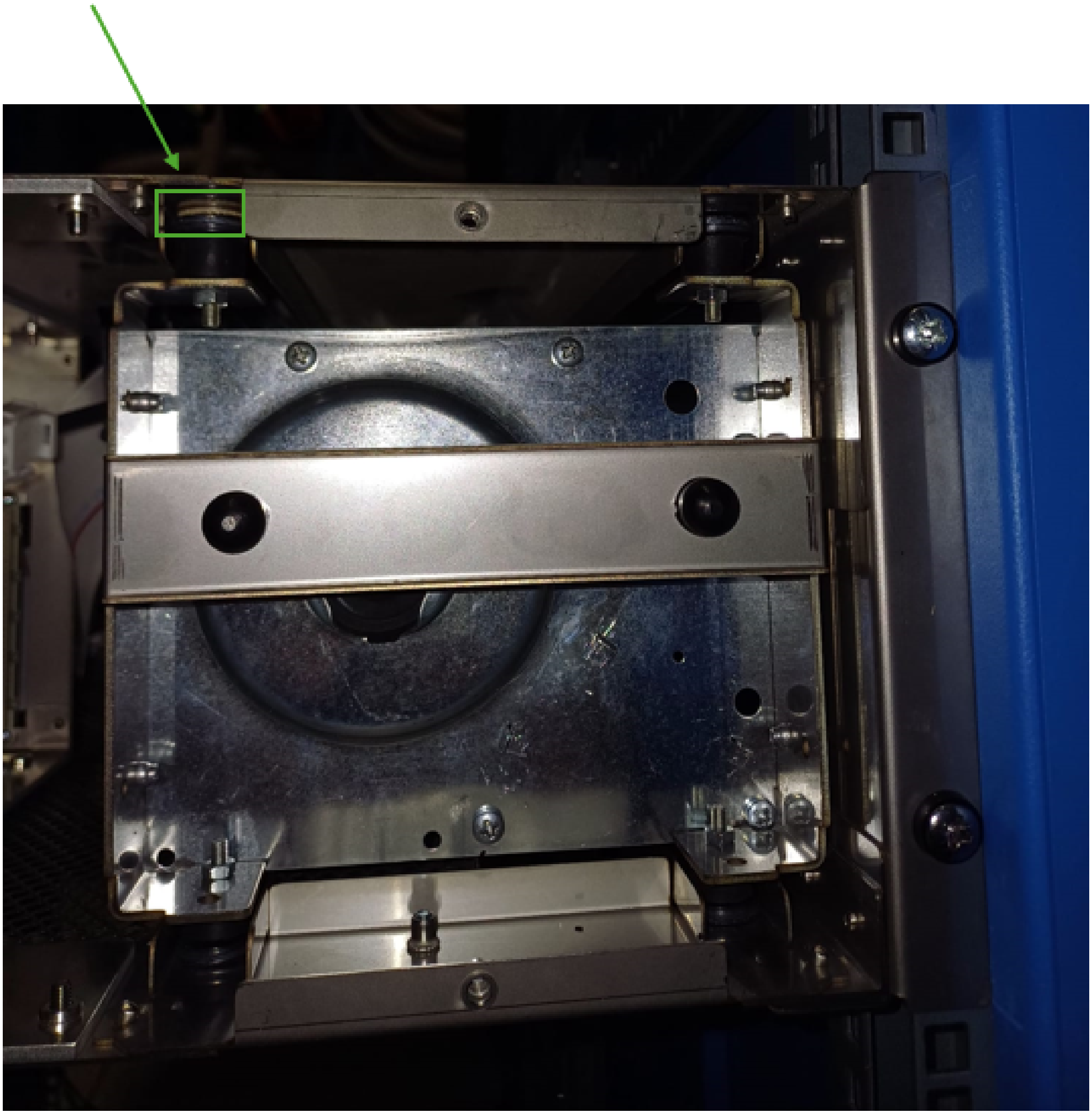

Figure 11.19: A photograph of the inserted spacer between the damper and the chassis.

Based on these results, any visible support gap should be eliminated during assembly. A shim, spacer, or equivalent filler material may be permanently bonded either to the damper or to the chassis support in order to ensure repeatable contact conditions.

11.5.2 Final Validation of the Revised Wheel Assembly

Following implementation of the spacer/shim solution and controlled assembly procedures, vibration measurements were repeated at all predefined measurement locations.

Figure 11.20 compares the final prototype wheel assembly against the previous configuration.

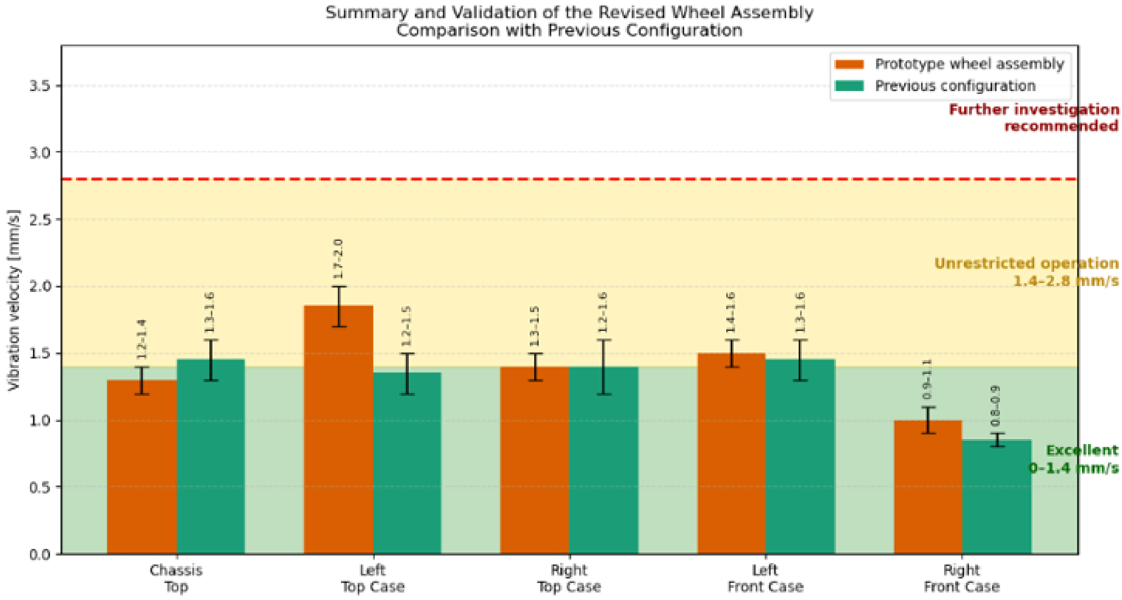

Figure 11.20: Final validation of the revised wheel assembly compared with the previous configuration.

The final prototype assembly achieved vibration levels comparable to those of the previous configuration at all measurement locations.

At the Chassis-Top location, vibration levels of approximately 1.2–1.4 mm/s were measured, slightly lower than the corresponding values obtained from the previous configuration. The case-front and right-side case-top locations also showed vibration levels comparable to those of the original system.

The left-side case-top measurement remained slightly higher, with values between approximately 1.7 and 2.0 mm/s. Nevertheless, these values remained within the unrestricted-operation range and were considered acceptable for the intended application.

The results demonstrate that the revised wheel assembly can be considered validated from a vibration perspective when installed using healthy motor/case assemblies and controlled assembly procedures. Furthermore, the investigation showed that assembly preload, local support conditions, and casing deformation can significantly influence the measured vibration response and must therefore be controlled through a repeatable assembly procedure.

Chapter 12

Conclusions

12.1 Summary of the Work

This thesis presented the integration and validation of a revised turbine assembly intended for use within the ATLAS electronics rack cooling system.

The work presented in this thesis will be implemented by the ATLAS Technical Coordination team and will be used to support the refurbishment and maintenance of the plastic ventilation system for ATLAS's electronics racks throughout the remaining operational lifetime of the LHC, currently planned until 2040.

The work included reverse engineering of existing components, CAD modelling, prototype preparation, assembly procedure preparation, development of a procurement strategy for target build quantity, airflow testing, vibration testing and validation of the revised wheel assembly.

Additionally, a systematic experimental campaign was conducted to identify the source of elevated vibration levels observed in the prototype and to verify the performance of the redesigned system.

12.2 Key Findings

The main findings of this work are summarized below:

- The revised wheel assembly maintained airflow performance comparable to the original configuration.
- Current and supply voltage measurements showed that both prototype and previous-configuration motors operated under comparable electrical conditions.
- Initial prototype vibration levels were significantly higher than those of the previous configuration.

- Bonding the bearing inner ring to the shaft produced only a minor improvement and was not identified as the primary source of vibration.
- High vibration levels persisted after removal of the turbine wheels, demonstrating that the wheel assembly was not the dominant source of excitation.
- Motor/case swap tests showed that elevated vibration followed the refurbished motors rather than the prototype case, revealing a complex interaction between the case and the motor.
- Assembly preload, case distortion and local support conditions significantly influenced vibration behaviour.
- Eliminating a local support gap reduced vibration levels significantly.
- The revised wheel assembly was successfully validated using healthy motor/case assemblies from the previous configuration.
- Final vibration levels were comparable to those measured for the original system.

The results demonstrate that the revised wheel assembly satisfies the functional requirements of the application and can be considered successfully validated from both airflow and vibration perspectives.

Chapter 13

Future Work

13.1 Potential Improvements, Further Testing&Optimization

Although the revised wheel assembly was successfully validated, several opportunities for further improvement were identified.

The most significant opportunity concerns the refurbished motor assemblies. Future experimental work should focus on optimization of the vibration response of the refurbished motor assemblies while maintaining the validated wheel design and assembly procedure.

Recommended activities include:

- Replacement of the healthy motors used during the wheel validation campaign with the refurbished motor assemblies, followed by repetition of the vibration measurements in order to quantify the contribution of the refurbished motors.
- Permanent implementation of the spacer solution identified during the validation campaign by bonding a shim, spacer, or equivalent filler material at the location of the support gap.
- Repetition of the vibration measurements after installation of the permanent spacer solution.
- If elevated vibration levels persist, further investigation of the motor refurbishment process should be performed, including evaluation of motor cleaning procedures, bearing installation methods, assembly tolerances, and other internal motor components that may influence vibration behaviour.
- Repetition of the vibration measurements following any modifications to the refurbishment procedure.

- If vibration levels remain significantly higher than those obtained with the unused motors, dynamic balancing of the refurbished motor assemblies should be considered.

These investigations would provide a deeper understanding of the dynamic behaviour of the refurbished motor assemblies and support further reduction of vibration levels while maintaining the validated performance of the revised wheel assembly. Additionally, long-term operational testing of the revised assembly under representative operating conditions would contribute to validation of the required 5 year lifetime of the system.

Bibliography

[1] ATLAS Collaboration. Atlas experiment at cern, 2024. URL: `https://www.atlas.ch`.

[2] Changqing Bai, Hongyan Zhang, and Qingyu Xu. Effects of axial preload of ball bearing on the nonlinear dynamic characteristics of a rotor-bearing system. *Nonlinear Dynamics*, 53(1-2):173–190, 2008. `doi:10.1007/s11071-007-9306-2`.

[3] CERN. Cern - the european organization for nuclear research, 2024. URL: `https://home.cern`.

[4] CERN ATLAS Experiment, Stephane Brachet. Internal technical drawings for ventilation system, 2025. Internal documentation.

[5] CERN ATS News. The long shutdown 3, 2025. Accessed: 2026. URL: `https://ats-news.web.cern.ch/the-long-shutdown-3/`.

[6] Geraldine Thomas. Lhc rack cooling measurements, 2003. URL: `https://cds.cern.ch/record/38031`.

[7] International Organization for Standardization. Mechanical vibration – evaluation of machine vibration by measurements on non-rotating parts – part 1: General guidelines. Technical Report ISO 10816-1:1995, International Organization for Standardization, Geneva, Switzerland, 1995.

[8] International Organization for Standardization. Mechanical vibration – measurement and evaluation of machine vibration – part 1: General guidelines. Technical Report ISO 20816-1:2016, International Organization for Standardization, Geneva, Switzerland, 2016.

[9] Longwell. Technical drawings for ventilation chassis components, 2025. Supplier-provided documentation, not publicly available.

[10] Karla H. Muci-Küchler et al. Simplified procedure for vibration analysis and dynamic balancing in mechanical systems with beats frequency. *Measurement*, 183:109056, 2021. `doi:10.1016/j.measurement.2021.109056`.

[11] SKF Group. Rolling bearings catalogue, 2023. URL: https://www.skf.com.

[12] John S. Steinhart and Stanley R. Hart. Calibration curves for thermistors. *Deep Sea Research and Oceanographic Abstracts*, 15(4):497–503, 1968. doi:10.1016/0011-7471(68)90057-0.

[13] Unknown. Ziehl abegg cross flow fans catalog, dl 6.1 - d/gb. URL: https://doczz.net/doc/5806924/querstromventilatoren-crossflow-fans.